Prototype cantilevers for quantitative lateral force microscopy

Mark G. Reitsma, Richard S. Gates, Lawrence H. Friedman, and Robert F. Cook
Nanomechanical Properties Group, National Institute of Standards and Technology, Gaithersburg, Maryland 20899, USA

Prototype cantilevers are presented that enable quantitative surface force measurements using contact-mode atomic force microscopy (AFM). The "hammerhead" cantilevers facilitate precise optical lever system calibrations for cantilever flexure and torsion, enabling quantifiable adhesion measurements and friction measurements by lateral force microscopy (LFM). Critically, a single hammerhead cantilever of known flexural stiffness and probe length dimension can be used to perform both a system calibration as well as surface force measurements *in situ*, which greatly increases force measurement precision and accuracy. During LFM calibration mode, a hammerhead cantilever allows an optical lever "torque sensitivity" to be generated for the quantification of LFM friction forces. Precise calibrations were performed on two different AFM instruments, in which torque sensitivity values were specified with sub-percent relative uncertainty. To examine the potential for accurate lateral force measurements using the prototype cantilevers, finite element analysis predicted measurement errors of a few percent or less, which could be reduced via refinement of calibration methodology or cantilever design. The cantilevers are compatible with commercial AFM instrumentation and can be used for other AFM techniques such as contact imaging and dynamic mode measurements. [doi:10.1063/1.3624700]

I. INTRODUCTION

The atomic force microscope (AFM) has become a primary research tool for small-scale surface and material property measurements in physical, chemical, biological, and medical application areas, including nanotechnology and biotechnology, as well as in the development of small-scale devices, such as microelectromechanical systems (MEMS). The key capability of AFM to resolve small-scale surface forces—ranging from micronewtons to piconewtons—across a multitude of material types and environments has led to the widespread use of AFM as a powerful measurement tool for applications in which surface forces phenomena can potentially dominate system behavior and properties. For instance, the development of functional class III and IV MEMS devices (i.e., those with contacting and moving components),[1] certain new and existing data storage technologies,[2] as well as the formation and manipulation of nanostructures on surfaces[3] are examples of applications in which nanoscale friction and adhesion phenomena can be critical to structure, operation, functionality, and control. Along with growing demand for enhanced sophistication and reliability of small-scale technologies will come measurement needs that include calls for base-unit-traceable accuracy in small-force measurement. The distinct lack of accurate small-scale force measurement procedures is progressively gaining ground as an issue and much recent effort has been focused on developing *precise* and *accurate* techniques for normal surface force measurement using optical lever AFM and related techniques.[4] The current paper extends this effort to AFM lateral force measurement and the quantification of sliding friction forces in the micro- to nano-scale range.

The AFM measurement technique known as lateral force microscopy (LFM) is the principal experimental method used

in the study of friction, adhesion, and lubrication phenomena at the nanoscale (i.e., "nanotribology"), with surface force measurement sensitivity that typically ranges from hundreds of micronewtons to hundreds of piconewtons. A LFM friction measurement is depicted in Fig. 1(a), in which a cantilever probe is in contact with a surface and an instrument-generated relative displacement of the probe and surface, ΔY, produces a lateral resistance force, F_Y, caused by friction at the contact interface. The friction force couples with the probe lever-arm of length h and the cantilever twists by an angle ϕ about its long (x) axis. The twist causes a laser spot (reflected from the back of the cantilever) to displace laterally (horizontal in Fig. 1(a)) on the AFM instrument split-quadrant optical position sensitive detector (quad-cell PSD), resulting in a change in lateral deflection output, ΔV_L. Repeated back and forth ΔY motion produces a hysteretic "friction-loop," with a half-width (ΔV_L) proportional to F_Y. The essential calibration requirement—to make LFM friction measurements quantitative—is to generate a sensitivity parameter for the combined cantilever and optical system ("optical lever system") that connects ΔV_L to F_Y in a precise and accurate manner.

During a LFM friction measurement, the application of a lateral force, F_Y, on the cantilever probe is always associated with a normal force, F_Z, which causes the cantilever to deflect flexurally. Fig. 1(b) shows a "force-displacement" measurement, in which an instrument-generated displacement ramp, ΔZ, brings a cantilever probe and an opposing surface into contact (during "approach" motion) and then out of contact again (during "retract" motion). The probe-surface interaction produces flexural deflection of the cantilever through an angle θ about its short (y) axis, which causes the laser spot to displace on the instrument PSD (vertical in Fig. 1(a)),
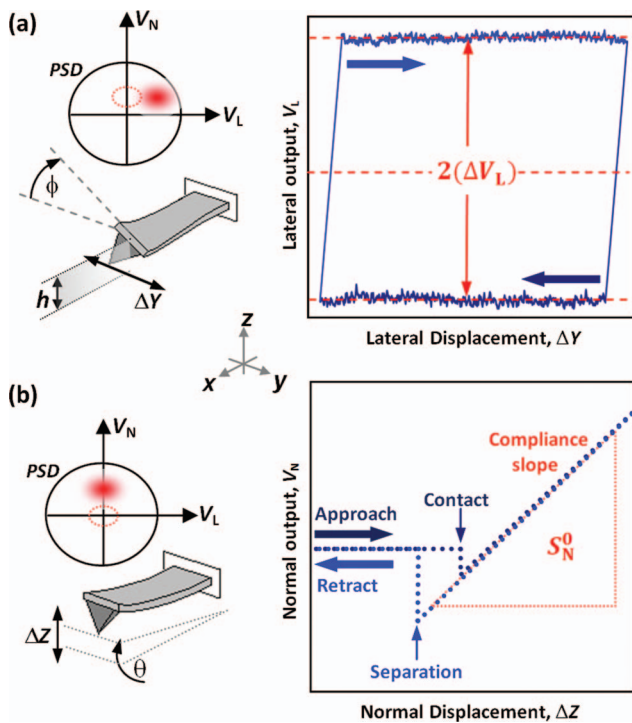
FIG. 1. (Color online) AFM quasi-static force measurements: (a) Depiction of a LFM friction measurement, in which a cantilever probe is in contact with a surface, and relative displacement, ΔY, produces a frictional resistance force (F_Y) that couples with the probe lever-arm of length h, such that the cantilever twists, ϕ, resulting in a lateral output response, ΔV_L, depicted as horizontal displacement of the laser spot on the position sensitive detector (PSD); repeated back and forth ΔY motion generates a "friction-loop." (b) Depiction of a "force-displacement" ramp, in which approach and retract, ΔZ, relative displacement, causes flexural deflection of the cantilever, θ, and a normal output response, ΔV_N, depicted as vertical displacement of the laser spot on the PSD; during contact between the cantilever probe and surface, the "compliance slope" gives the normal sensitivity, S_N^0, of the optical lever system.

resulting in a change in normal deflection output, ΔV_N. While the cantilever probe is in contact with the opposing surface, approach and retract motion generates a "compliance slope," S_N^0, which is used as the normal displacement sensitivity of the optical lever system. Quantification of the normal force acting on the probe, F_Z, at a given displacement, ΔZ, involves knowledge of the cantilever flexural stiffness, k_Z, as well as of S_N^0. Over the past two decades, many studies have been devoted to the measurement of AFM cantilever flexural stiffness,[4,5] and to the interpretation of force-displacement data,[6] such that these measurements are often conventionally regarded as routine, despite some remaining challenges to quantitative interpretation.[4,7,8] As for normal surface force measurements, LFM friction force measurements have also been investigated for around two decades,[9] but the practical realization of calibration parameters for a cantilever torsional response is a more complicated problem (compared to a flexural response), and there remains no definitive consensus on an approach for quantitative LFM measurements of friction, although several methods have been the subject of evaluation and refinement.[10]

The "pivot" LFM calibration techniques of Bogdanovic *et al.*[11] and of Feiler *et al.*[12] induce simultaneous flexure and twist in the cantilever, in which the flexural component of the

cantilever response is used to calibrate the optical lever system for force and torque on the cantilever. That is, the cantilever is loaded in the same fashion as it is for "simple" flexure, via a ΔZ displacement ramp, as in Fig. 1(b), but the load is offset from the central axis of the cantilever (in the y-direction). The offset causes the cantilever to undergo flexure and twist simultaneously, which produces both normal, ΔV_N, and lateral, ΔV_L, deflection outputs from the PSD. The assumption is that, for small deflections, the flexural and torsional deformation responses of the cantilever are mechanically in-series, but decoupled. The measured twist response of the optical lever system, ΔV_L, can thus be related to torque applied to the cantilever via the product of a calculable force, F_Z (via k_Z and S_N^0), and the distance at which the force is applied from the shear center of the cantilever, about which twisting occurs (see later). Bogdanovic *et al.*[11] loaded the cantilever by engaging it with a protrusion on a surface during ΔZ displacement ramping. Feiler *et al.*[12] glued a stiff beam to the free-end of the cantilever (orthogonal to its long-axis) and engaged the free-end of the attached beam with an opposing surface during a ΔZ displacement ramp; the extended lever-arm generated a greater PSD signal-to-noise ratio, as there was greater torque on the cantilever. Regardless of the loading method, the data analysis method of Feiler *et al.*[12] provides for a very robust calibration of the PSD response to cantilever force and torque when used to perform a pivot calibration consisting of multiple lever-arm measurements.[13,14]

AFM force calibration methods that offer the greatest potential for accuracy are those that can be performed *in situ*, along with force measurements, without disturbing the optical lever system between calibration and measurement. A significant disadvantage of the loading method used by Feiler *et al.*[12] is that it cannot be performed readily *in situ*, as the beam must be attached or removed from the cantilever between calibration and measurement. The *in situ* pivot loading approach of Bogdanovic *et al.*[11] was recently tested and refined in a study that performed pivot calibrations using various commercially available rectangular cantilevers. The study highlighted a limitation in obtainable precision attributed to the spatial constraints of typical rectangular AFM cantilevers (i.e., they are narrow).[14] In another pivot calibration approach, a T-shaped cantilever geometry was proposed as a means of combining the extended lever-arm approach of Feiler *et al.* with the *in situ* loading procedure of Bogdanovic *et al.* The study demonstrated that a sensitive and precise *in situ* pivot calibration could be obtained for cantilever torsion across the working range of the PSD relevant to friction measurements, but it required construction of a cantilever with a T-shaped ("hammerhead") geometry near the probe.[13]

This paper presents a microfabricated T-shaped hammerhead cantilever that delivers a precise instrument calibration for quantitative micro- to nano-scale normal and lateral (friction) force measurements. Section II describes AFM force measurement principles relevant to the pivot LFM calibration technique and its implementation using hammerhead geometry cantilevers. Section III presents experimental methods and results: Sec. III A describes the fabrication procedures used to construct hammerhead cantilevers—a single hammerhead cantilever was chosen for use in all experiments

reported in this paper; Sec. III B presents a stiffness property characterization of the selected hammerhead cantilever using instrumented indentation direct force-displacement measurements; Sec. III C describes the physical implementation of hammerhead pivot measurements, in which the selected hammerhead cantilever was used to examine method *precision* by performing pivot calibrations on two distinct AFM instrument platforms. As a further analysis, AFM pivot data were used to generate torsional stiffness values for the hammerhead cantilever (used on both AFM instruments), which could be also compared with the torsional stiffness value obtained via instrumented indenter (for the same cantilever). Section IV presents a finite element analysis of hammerhead cantilever mechanics, with a focus on underlying assumptions regarding the *accuracy* potential of the LFM pivot calibration method using a hammerhead cantilever. Discussion in Sec. V considers advantages and limitations of the hammerhead pivot technique and how it could be further improved.

II. FORCE CALIBRATION AND MEASUREMENT

In the following, AFM quasi-static force measurement principles relevant to the LFM pivot calibration technique are described in Sec. II A. In Sec. II B, pivot loading of a hammerhead cantilever is described, in which the calibration of an optical lever torque sensitivity (for the quantification of LFM friction data) is discussed in Sec. II B 1, and the measurement of torsional stiffness of a pivot loaded hammerhead cantilever is discussed in Sec. II B 2.

A. Normal and lateral force measurements

Practically, the application of a LFM lateral force, F_Y, is always associated with some normal applied force, F_Z. In fact, F_Y is usually interpreted as a function of F_Z. Fig. 1(b) depicts relative displacement, ΔZ, of a cantilever probe and opposing surface, so as to generate simple flexural deflection (rotation) of the cantilever by an angle, θ, out of its plane and a resulting normal force at the surface, $F_Z = k_\theta \theta$, where k_θ is the rotational stiffness of the cantilever.[8] Flexural deflection of the cantilever produces a normal deflection PSD output, ΔV_N, proportional to θ. Small flexural cantilever deflections are proportional to force,[15] and thus ΔV_N is a measure of the probe-surface normal interaction force, F_Z. The deflection generates a displacement of the cantilever, w, in the z-direction. For small deflections, w is proportional to θ, and the flexural stiffness (normal spring constant) of the cantilever, k_Z, is given by $F_Z = k_Z w$. For conditions in which the combined probe-surface-contact stiffness,[16] k_Z^c, is very large ($k_Z^c \gg k_Z$; see later), normal deformation in the vicinity of the probe-surface interface is negligible, $w \approx \Delta Z$, and

$$F_Z = k_Z \Delta Z. \tag{1}$$

Under these conditions, the normal sensitivity of an optical lever system, S_N^0, is given by the compliance slope of a force-displacement ramp (see Fig. 1(b)), such that

$$\Delta V_N = S_N^0 \Delta Z, \tag{2}$$

where the 0 superscript in S_N^0 indicates that the normal force is applied with zero offset from the shear center of the cantilever

(i.e., there is nominally zero torque applied about the long axis of the cantilever). Eqs. (1) and (2) give

$$F_Z = \left(k_Z / S_N^0 \right) \Delta V_N. \tag{3}$$

Once S_N^0 has been determined, knowledge of the cantilever flexural stiffness, k_Z, allows normal forces to be measured from the PSD normal output, ΔV_N. Surface adhesion from the snap-in "contact" and pull-off "separation" portions of force-displacement curves (Fig. 1(b)) are common quasi-static AFM normal surface force measurements.[6]

The lateral force, F_Y, applied at the probe-surface contact during a LFM experiment (via lateral displacement, ΔY) generates a torque, $T = F_Y h$, on the cantilever as F_Y couples to the probe moment arm of length h, which extends from the probe-surface contact (at the probe apex) to the shear center of the cantilever (about which twisting occurs). For fixed h, small cantilever twist is proportional to torque. As depicted in Fig. 1(a), as the cantilever twists, the laser spot moves laterally across the PSD and repeated back and forth ΔY motion in a LFM experiment generates a friction-loop. A typical friction-loop consists of four segments: two "dynamic friction" segments, in which average lateral deflection values (ΔV_L) are approximately invariant with ΔY; and two "static friction" segments. Prior to the onset of relative motion in a given ΔY direction, the response of the probe moment-arm is set by nominally static friction between the probe and the surface and the response is a lateral compliance. As ΔY, and thus F_Y, extend beyond a critical value, static friction is exceeded and the probe slides across the surface in dynamic (sliding) friction. A LFM measurement procedure involves the determination of the lateral deflection during dynamic friction by calculating the *difference*, ΔV_L, in lateral deflection between one sliding direction and the other—called the "friction-loop half-width"—which is proportional to the lateral friction force at the surface (i.e., $\Delta V_L \sim F_Y$). The example data in Fig. 1(a) show "noise" in the dynamic portions of the friction-loop, caused by changes in topography or energy dissipation pathways as the probe travels over the surface.[17] The method by which ΔV_L is calculated will thus depend on the focus of a particular experiment; for example, whether interest is in an averaged lateral response over an entire slide or in the fine details of interaction (e.g., atomic-scale stick-slip corrugations). In any case, a precise and accurate connection between ΔV_L and F_Y is required.

In the lateral compliance domain, the lateral force arising from the imposed surface displacement (ΔY) generates three cantilever-probe displacements. The first is associated with a lateral displacement of the cantilever axis in the x–y-plane, causing a sideways "in-plane" cantilever deflection,[18] with a displacement, v. The second is the deformation of the combined probe-surface-contact spring,[16,19] v_c. The third is the net displacement of the probe that produces twist in the cantilever, $v_Y = \Delta Y - v - v_c$. As displacements v and v_c do not lead to either flex (θ) or twist (ϕ) of the cantilever, for all practical purposes, they are not sensed by the instrument PSD. The displacement, v_Y, leads to twist, and for small twist, $\phi = v_Y / h$. The "torsional stiffness" of the cantilever, k_ϕ, relates torque to cantilever twist, and is given by $T = k_\phi \phi$. The cantilever "torque stiffness," k_T, relates lateral force to
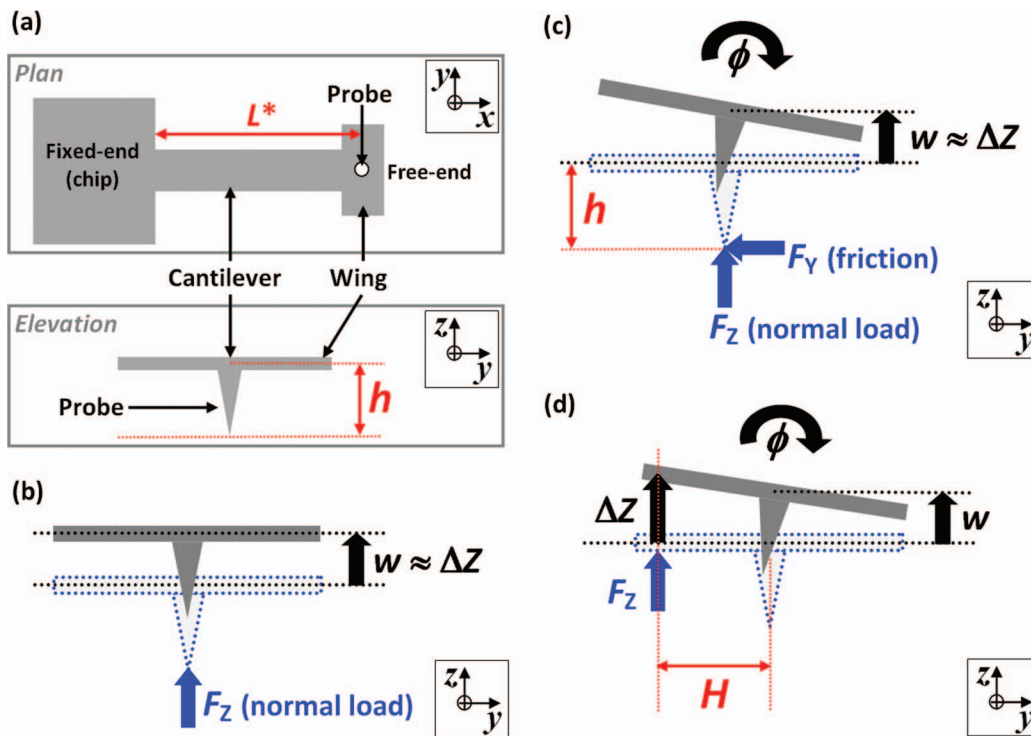
FIG. 2. (Color online) Application of F_Z and F_Y loads to a hammerhead cantilever via instrument-imposed displacements, showing: (a) Plan and elevation views of a hammerhead cantilever and probe; (b) Normal loading of the hammerhead cantilever; (c) Lateral (LFM friction) loading of the hammerhead cantilever; (d) Pivot loading of the hammerhead cantilever.

lateral probe apex displacement, and is given by $F_Y = k_T v_Y$, analogous to Eq. (1). For small twist, the two stiffness parameters are thus related by

$$k_T = (k_\phi / h^2). \tag{4}$$

In order to measure lateral forces related to frictional probe-surface interactions in LFM, a calibration procedure is required to relate F_Y to the lateral response, ΔV_L. An optical lever sensitivity parameter, called a "torque sensitivity," S_T, can be defined in terms of a known torque, T, applied to the cantilever to produce a lateral response, ΔV_L, such that

$$S_T = (\Delta V_L / T), \tag{5}$$

analogous to Eq. (2), and allowing the lateral friction force to be expressed as

$$F_Y = (\Delta V_L / S_T h), \tag{6}$$

analogous to Eq. (3). The following Section II B describes the AFM pivot calibration method for use with hammerhead cantilevers.

B. Hammerhead pivot measurements

Figure 2 illustrates the application of loads, F_Z and F_Y, to a hammerhead cantilever by way of instrument-imposed displacement. Figure 2(a) depicts plan and elevation views of the cantilever and probe, in which the effective length of the cantilever, L^*, extends from the fixed-end at the edge of the handling chip to the probe on the cantilever. The lateral extensions on either side of the probe are referred to as "wings." The probe has an effective length, h, extending from

the probe apex to the shear center of the cantilever. The shear center of the cantilever is conventionally assigned the location at the centroid of the cantilever's rectangular cross-section for all practically relevant lateral loads imposed on a hammerhead cantilever during LFM friction experiments (i.e., when sliding on approximately planar surfaces). This assumption is investigated later in Sec. IV D. In Fig. 2(b), a (normal) z-directed force, F_Z, is applied to the probe by "ΔZ ramping" through a vertical displacement, ΔZ, such that the cantilever deflects flexurally through a distance w. For conditions in which the probe-surface-contact stiffness (k_Z^c) is effectively rigid, $w \approx \Delta Z$. Figure 2(c) shows the load configuration for a LFM friction experiment, in which a normal force, F_Z, and a lateral force, F_Y, are applied simultaneously to the probe to generate simultaneous flex, $w \approx \Delta Z$, and twist, ϕ, of the cantilever. Figure 2(d) shows the load configuration for a pivot calibration, in which F_Z is generated by engaging the cantilever with a loading structure, called a "pivot" (typically an inverted tip or microsphere attached to an opposing surface). The distance, H, is defined along the y-axis from the position of the cantilever shear center to the load point on the wing. ΔZ ramping causes the cantilever to twist, ϕ, as well as flex through a displacement $w (\neq \Delta Z)$. For uncoupled flexural and torsional cantilever responses, torque is quantified as $T = F_Z H$, where $F_Z = k_Z w$.

Figures 1(b) and 2(b) show a ΔZ ramp imposed on a cantilever probe to generate *force-displacement* data from which the normal displacement sensitivity, S_N^0, can be obtained, as shown in Fig. 1(b). Figure 2(d) shows a ΔZ ramp imposed at H on a hammerhead cantilever wing to produce a *torque-displacement* response, also required for a hammerhead pivot
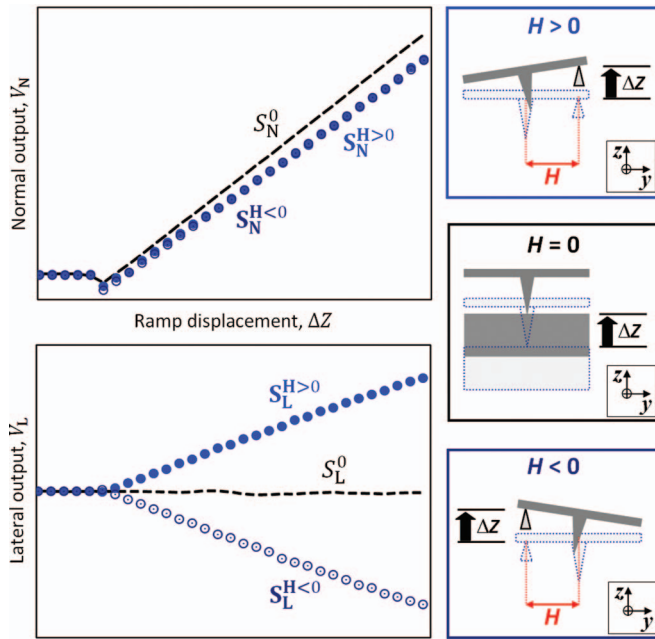
FIG. 3. (Color online) Hammerhead pivot calibration: the three types of cantilever loading and associated data. The dashed lines represent force-displacement loading ($H = 0$), implemented by ΔZ ramping of the cantilever probe against a flat surface, which produces normal and lateral compliance slopes, S_N^0 and S_L^0, respectively. Torque-displacement loading is implemented by ΔZ ramping the cantilever wing with a pivot (depicted as a tip) at a lever-arm distance H. The solid circles represent a $H > 0$ lever-arm, which gives the compliance slopes $S_N^{H>0}$ and $S_L^{H>0}$; the open circles represent a $H < 0$ lever-arm, which gives the compliance slopes $S_N^{H<0}$ and $S_L^{H<0}$.

calibration. The illustrations in Fig. 3 show the hammerhead cantilever engaging a pivot (depicted as a tip) for torque-displacement loading, and engaging a flat surface for force-displacement loading. Example data for force-displacement and torque-displacement loading are also shown in Fig. 3. A hammerhead pivot calibration involves three types of cantilever loading data: (1) force-displacement loading, with $H = 0$ (dashed lines); (2) torque-displacement loading for $H > 0$ lever-arms (solid circles); and (3) torque-displacement loading for $H < 0$ lever-arms (open circles). Note that since ΔZ displacements are small (nanometers) compared to cantilever dimensions (micrometers), H can be considered practically constant during ΔZ ramping. Each type of loading causes a response in both the normal output, V_N, and lateral output, V_L, of the instrument. It is the ratio of lateral to normal output responses—V_L per V_N—for each H that provide a pivot torque sensitivity calibration of the optical lever system (see later).

Force-displacement data provide an indication of the optical lever system alignment, and for the system shown in Fig. 3, good alignment is indicated by $S_L^0 \approx 0$ in the lateral response, meaning that the laser spot is tracking the sector axis of the PSD as the cantilever deflects flexurally (i.e., along the vertical, V_N, PSD axis in Fig. 1(b)). Good alignment in this system is also evident from the torque-displacement data for equal but opposite lever-arms, H, as both $S_N^{H>0}$ and $S_N^{H<0}$ traces overlap in the normal output and $S_L^{H>0}$ and $S_L^{H<0}$ traces are split in equal but opposite directions in the lateral output. In comparing the two types of optical lever responses, the ob-

servation that $S_N^H < S_N^0$ is expected, since the cantilever load-point displacement is accommodated by both flex and twist in the cantilever during torque-displacement loading (with $H \neq 0$), compared to only flex in the force-displacement loading case (with $H = 0$). It should be noted that good optical lever system alignment, as indicated by the system in Fig. 3, is not readily achieved in most AFM experimental setups, and a certain degree of optical misalignment is typical. Optical misalignment produces "crosstalk" between normal and lateral output channels, caused by misalignment between the cantilever reflective (beam bounce) surface and the sector axis of the PSD. Obvious signs of optical crosstalk are: force-displacement curves that generate a non-zero slope in the lateral output, $S_L^0 \neq 0$; for equal but opposite lever-arms, $|H > 0| = |H < 0|$, torque-displacement curves that do not overlap in the normal output ($S_N^{H>0} \neq S_N^{H<0}$), and do not split equally in the lateral output ($|S_L^{H>0}| \neq |S_L^{H<0}|$). The effect of crosstalk on the interpretation of force and torque in this calibration method is discussed later. Finally, note that the well-aligned optical lever system represented in Fig. 3 was obtained in experiments separate from all others in this paper.

The principal experimental exercise of this paper is to demonstrate the performance of a hammerhead cantilever pivot calibration in determining the torque sensitivity, S_T, of AFM optical lever systems with a high degree of precision. The following, Sec. II B 1, outlines the principles with which AFM pivot calibration data can be used to extract an optical lever system torque sensitivity, S_T. To provide further insight into the underlying metrology of the pivot method and mechanics of the hammerhead cantilever in use, Sec. II B 2 outlines the measurement of the cantilever torsional stiffness, k_ϕ, from AFM pivot calibration data, as well as a possible means for measuring k_ϕ using a force-displacement measurement instrument, such as an instrumented indenter.

1. Torque sensitivity

If the compliance elements controlling cantilever flexure and twist are uncoupled, then the normal and lateral detector responses may be treated independently to assess force and torque on the cantilever. From Eqs. (3) and (5), and recognizing that the torque on the cantilever in a pivot measurement is $T = F_Z H$ (see Fig. 2(d)), then

$$\Delta V_N = \frac{S_N^0}{k_Z} F_Z, \tag{7a}$$

$$\Delta V_L = S_T T = S_T F_Z H. \tag{7b}$$

Eliminating F_Z in Eq. (7) gives

$$\left(\frac{\Delta V_L}{\Delta V_N}\right) = H \left(\frac{k_Z}{S_N^0}\right) S_T. \tag{8}$$

If k_Z is known and S_N^0 is determined from force-displacement measurements, then measurement of the detector output ratio ($\Delta V_L / \Delta V_N$) as a function of H enables S_T to be determined from Eq. (8). This provides a calibration of the integrated mechanical and optical sensitivity of the instrument, such that frictional forces can be measured through the use of Eq. (6). An additional contribution to uncertainty in determination of

the torque sensitivity comes from the fact that k_Z is typically quantified in a separate calibration procedure (*ex situ*). However, all other parameters in Eq. (8) are determined *in situ*, including S_N^0, which is quantified from force-displacement measurements by setting $H = 0$.

The S_T value of an AFM optical lever system is the calibration parameter used to quantify LFM friction force (friction-loop) data, by way of Eq. (6). A cantilever torsional stiffness value is not required for the measurement of LFM friction forces in this case. However, the data that are collected for a pivot S_T calibration also provide a value of the cantilever's torsional stiffness, k_ϕ. The study reported here includes an analysis of cantilever k_ϕ measurements from pivot calibration data in order to facilitate a deeper understanding of the metrology underlying the method.

2. Cantilever torsional stiffness

Assuming the contact between the pivot and cantilever to be rigid, the loading depicted in Fig. 2(d) suggests three cantilever compliances for consideration. The first compliance, k_Z^{-1}, is associated with flexural deflection of the cantilever, w, determined at L^*. The second compliance, k_ϕ^{-1}, is associated with torsional deflection of the cantilever, ϕ, also determined at L^*, where $k_T^{-1} = k_\phi^{-1} H^2$ is obtained by setting $h = H$ in Eq. (4). The third is the compliance of the lateral wing of the cantilever, $(k_Z^H)^{-1}$, over a distance H. If the wing has a very small compliance relative to the flexural and torsional cantilever springs (i.e., $k_Z^H \gg k_Z, k_T$), where k_Z and k_T are assumed to be separable and can be treated as uncoupled elastic elements in series, the displacement of the load point is linearly related to the applied force by

$$F_Z = k_Z^{\text{tot}} \Delta Z, \tag{9}$$

where k_Z^{tot} is given by

$$\left(k_Z^{\text{tot}}\right)^{-1} = (k_Z)^{-1} + (k_T)^{-1} = (k_Z)^{-1} + (k_\phi)^{-1} H^2. \tag{10}$$

Equation (10) suggests a means to measure the combined flexural-torsional stiffness of a cantilever, k_Z^{tot}, using an apparatus such as an instrumented indenter and associated techniques to measure the flexural stiffness of AFM cantilevers, described elsewhere.[20,21] That is, if the instrumented indenter were used to apply pivot loads to a hammerhead cantilever, by ΔZ ramping over a range of H values (at L^*), while measuring F_Z directly, then it should be possible to determine k_Z and k_ϕ using Eq. (10). In principle, such measurements could provide a traceable determination of cantilever stiffness properties.

Provided k_Z is known, then k_ϕ can also be determined via an AFM pivot calibration. As shown in Fig. 3, torque-displacement loading of linear elastic cantilever compliance elements will generate normal and lateral detector responses that should be linearly related to the imposed ramp displacement, such that

$$\Delta V_N = S_N^H \Delta Z, \tag{11a}$$

$$\Delta V_L = S_L^H \Delta Z. \tag{11b}$$

Combining Eqs. (7a), (9), (10), and (11a) gives

$$\frac{S_N^0}{S_N^H} - 1 = H^2 \left(\frac{k_Z}{k_\phi}\right), \tag{12}$$

which provides a method for determining k_ϕ from AFM pivot measurements by observing the ratio of normal sensitivities as a function of H.

III. EXPERIMENTAL METHODS AND RESULTS

This section describes the experiments conducted and results obtained for AFM pivot loading of a prototype hammerhead cantilever. In Sec. III A, the procedures used to fabricate hammerhead cantilevers are described. From the wafer batch of cantilevers produced, a single hammerhead cantilever was selected as the subject of all experimental measurements. In Sec. III B, the flexural and torsional stiffness values of the cantilever were measured using an instrumented indenter. Section III C describes the physical implementation of pivot calibrations using the selected hammerhead cantilever: in Sec. III C 1, torque sensitivity calibrations were performed on two distinct AFM instrument platforms; in Sec. III C 2, pivot calibration data are used to determine the torsional stiffness of the cantilever, as measured on the two AFM instrument platforms, and compared with the torsional stiffness value determined from instrumented indentation measurements (from Sec. III B).

A. Fabrication of prototype hammerhead cantilevers

Scanning electron microscope (SEM) images of the prototype hammerhead device are shown in Fig. 4, with a typical "chip" in a wafer carrying two cantilevers with nominal lengths (x-dimension) $L = 500\,\mu$m and $L = 300\,\mu$m, from the fixed end at the chip edge to the cantilever free-end. Both types of cantilever have nominal dimensions of $6\,\mu$m thick (z-dimension) and $50\,\mu$m wide (y-dimension). The cantilever long-axis (x-dimension) and wing axes are aligned along the Si $\langle 110 \rangle$ directions. A $300\,\mu$m cantilever was the subject of all experimental measurements reported in this study.

The hammerhead cantilevers were microfabricated using a combination of contact optical lithography and deep reactive ion etching (DRIE) of silicon-on-insulator (SOI) wafers. The use of SOI allowed the buried oxide (BOx) layer between the SOI device layer and the handle wafer to serve as an etch stop during DRIE, which provided reasonably good control over the cantilever thickness for different devices on a wafer. The 100 mm diameter Si (100) SOI wafer used here had a nominal device layer thickness of $6\,\mu$m with a $1\,\mu$m BOx layer and a $400\,\mu$m handle wafer thickness. The plan dimensions of the cantilevers and chip were defined by contact optical lithography using a positive photoresist. Fiducial marks on the chip were patterned as part of the front side mask and etched out at the same time as the cantilevers. Subsequent removal of Si from the device layer was accomplished using DRIE, with the resist serving as a protective mask over device areas of the wafer. When etching had proceeded through the entire device layer to the underlying buried oxide, etching was stopped. A second resist layer was then applied to the back
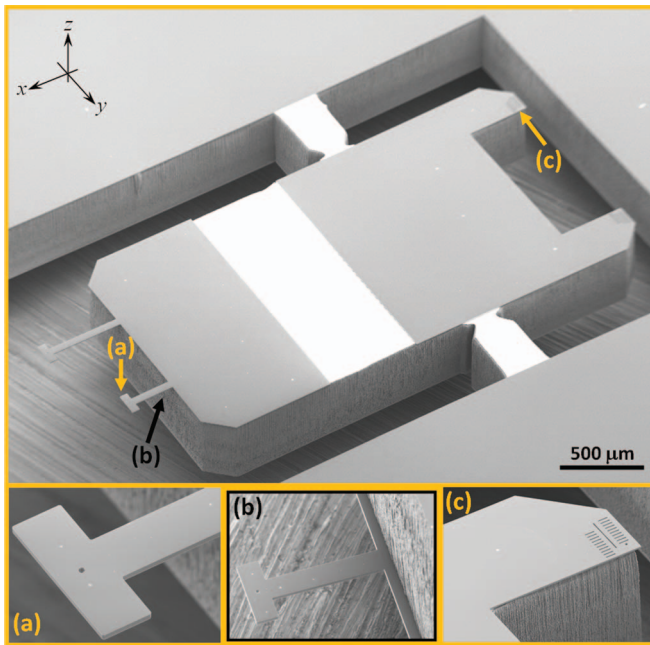
FIG. 4. (Color online) Scanning electron microscope images of the prototype hammerhead cantilever chip. The main picture shows the chip in a wafer, carrying two cantilevers: one 500 μm long and the other 300 μm long; both cantilevers are nominally 6 μm thick and 50 μm wide. Inset (a) shows a hammerhead cantilever "head" without probe. Inset (b) shows an underside view of a cantilever, revealing an approximately 25 μm undercut, resulting from imperfect vertical side-wall etching during fabrication. Inset (c) shows a "ramp dock" area of a chip, with 10 μm increment fiducial marks that are used in calibration.
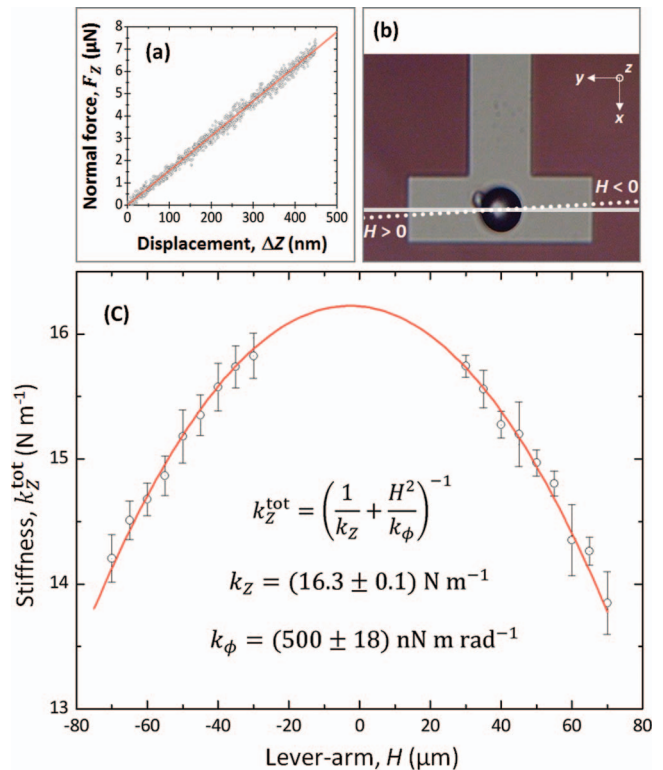

FIG. 5. (Color online) Instrumented indenter stiffness measurements made across the head of the hammerhead cantilever. (a) Representative data for an indenter force-displacement measurement. (b) Optical microscope image of the cantilever with tungsten sphere as the colloidal probe; overlaid on the image is a depiction of the misalignment between the cantilever axis (solid line) and indenter loading axis (dotted line). (c) Indenter measurements as a function of position, H, across cantilever head; the solid line is a fit to the data assuming an elements (k_Z, k_ϕ) in series (flex and twist) cantilever response.

of the wafer and patterned using contact optical lithography. Back side alignment was used to align the back side pattern (the chip design) to the front side cantilevers. DRIE through the back side proceeded through the handle wafer until the BOx layer was reached. At that point, the etching process was stopped, resulting in a clearly defined chip. A final wet etch in hydrofluoric acid was used to remove the exposed buried oxide, which released the cantilevers. The final thickness of the device layers for the SOI (corresponding to the thickness of the cantilevers) was measured to be $(5.8 \pm 0.2)\,\mu$m using a white light interferometric microscope.[22] The chip design included two "notched" legs midway along the chip (shown in Fig. 4). This insured that the chip was securely held in place during microfabrication and could be snapped out of the wafer for use.

The cantilevers were fabricated without integrated tips so that microspheres could be attached for use as probes (see later). A hammerhead cantilever "head" is shown in Fig. 4(a), where a fiducial "center-head" marker can be seen in the center of the head to guide positioning of microsphere attachment. The wings extend 75 μm from the center-head marker. Figure 4(b) shows an underside view of a representative cantilever that reveals an undercut shelf at the fixed-end. Undercutting occurred during DRIE of the chip from the back side. The slight deviation from a perfect 90 degree DRIE sidewall was accentuated by the extreme depth of the etch through the silicon (400 μm), such that when completed, the front and back side etches met with an overlap that was estimated to be 25 μm from SEM images. Figure 4(c) shows the back end

of the chip, which consists of "ramp dock" areas with 10 μm increment fiducial marks that are used in the calibration (described in Sec. III C).

B. Indenter measurements

Figure 5 shows direct stiffness measurements of a hammerhead cantilever using an instrumented indenter. Figure 5(a) shows representative indenter force-displacement data, composed of 1024 data points collected for typical indenter displacements, ΔZ, of 400 nm to 500 nm. The measured stiffness values, k_Z^{tot}, were determined from the slopes of the force-displacement data (as in Fig. 5(a)), obtained using least-squares linear fitting.[23] Figure 5(b) shows the hammerhead cantilever used for all experimental work. It was constructed as a "colloidal probe" by epoxy gluing a tungsten sphere onto the center-head marker of the cantilever head (see Fig. 4(a)). The sphere diameter was measured to be $(25.9 \pm 0.2)\,\mu$m using a white light interferometric microscope.[22] A small patch of the epoxy resin, used to glue the sphere to the cantilever, can be seen on the cantilever near the upper left-hand-side of the sphere in Fig. 5(b). Figure 5(c) shows instrumented indenter measured stiffness, k_Z^{tot}, versus lever-arm distance, H. Data symbols in Fig. 5(c) represent the mean and standard deviation of five non-sequential repeat force-displacement measurements (as in Fig. 5(a)) at

TABLE I. Experimentally determined cantilever and optical lever system properties.

| Instrument	Cantilever property		Optical lever system property	
	Flexural stiffness, k_Z (N m^{-1})	Torsional stiffness, k_ϕ (nN m rad^{-1})	Normal sensitivity, S_N^0 (V μm^{-1})	Torque sensitivity, S_T (V nN^{-1} m^{-1})
Instrumented Indenter	16.3 ± 0.1	500 ± 18	N.A.	N.A.
AFM Instrument A	N.A.	503 ± 17	13.40 ± 0.02	6.14 ± 0.01
AFM Instrument B	N.A.	471 ± 10	3.59 ± 0.01	0.169 ± 0.001

each lever-arm distance, H, across the head of the hammerhead cantilever (at a distance L^* along the cantilever length). For the determination of H values, the estimated uncertainty in instrument positioning of the indenter probe on the cantilever ($\pm 2\,\mu$m) is smaller than the symbol size. Lever-arm measurements less than $H = \pm 30\,\mu$m were not recorded due to mechanical interference or slippage between the indenter probe and the cantilever probe. Figure 5(c) shows an asymmetry about $H = 0$ in the measured stiffness (e.g., compare k_Z^{tot} values for $H = -70\,\mu$m with $H = +70\,\mu$m), which was caused by a small misalignment ($\approx 1°$) between the axis of the cantilever (depicted by solid line in Fig. 5(b)) and the indenter positioning stage axis (depicted by dotted line in Fig. 5(b)). This resulted in $H < 0$ measurements that were made closer to the cantilever fixed end (generating a greater stiffness) than $H > 0$ measurements (generating less stiffness). The solid line on the plot in Fig. 5(c) represents the results of a linear least-squares fit of the data to the springs-in-series model, Eq. (10), providing stiffness values for the hammerhead cantilever of $k_Z = (16.3 \pm 0.1)$ N m^{-1} and $k_\phi = (500 \pm 18)$ nN m rad^{-1}. These values are also listed in Table I. To calculate these values, the average measured stiffness at each H was fit in linearized coordinates of Eq. (10), $(k_Z^{\text{tot}})^{-1}$ and H^2, where associated statistical uncertainties of the fit parameter stiffness values are given as the standard errors of the fit.[23] Note that the uncertainties quoted for these measurements represent statistical uncertainties that do not include a potential measurement uncertainty (up to about 5%) in the force-displacement accuracy of the indenter instrument used here.[21] Another consideration is the stiffness of the contact between the indenter tip and cantilever: for a typical contact load of $5\,\mu$N and an indenter tip radius of about $3\,\mu$m, the Hertzian contact stiffness is approximately 12.5 kN m^{-1}, about three orders of magnitude greater than the flexural stiffness of the cantilever, showing that the required condition, $k_Z^{\text{c}} \gg k_Z$, is met, and that contact deformation is negligible relative to flexural deformation of the cantilever.[16] Approximate guidance from beam theory gives flexural and torsional stiffness values of $(15.3 < k_Z < 19.9)$ N m^{-1} and $(502 < k_\phi < 547)$ nN m rad^{-1}, respectively, using elastic constants appropriate to extension in the [110] direction and shear in the (110) plane,[24] for a rectangular silicon beam with dimensions of width $= 50\,\mu$m, thickness $= 5.8\,\mu$m, and bounds on the effective length, $(300 > L^* > 275)\,\mu$m, based on the apparent x-dimension of the undercut shelf from SEM images (see Fig. 4(b); Sec. III A). Although these calculations are estimates, the beam theory exercise also serves to emphasize that

techniques relying on dimensional measurements to describe the mechanical behavior of AFM cantilevers can be susceptible to significant errors arising from those measurements. In this case, the extent to which the undercut shelf formed part of the effective cantilever length, and the position and extent to which the shelf itself could be regarded as "pinned" to the chip, was not clear. Referring to Eq. (8), uncertainty in the determination of k_Z directly propagates to uncertainty in the determination of optical lever torque sensitivity, S_T, for the measurement of lateral forces (obviously, it propagates to uncertainty in normal forces as well, Eq. (3)). The instrumented indenter k_Z value determined here was associated with a very low statistical uncertainty, demonstrating good precision. Considerably more involved would have been an accurate (SI-traceable) determination of k_Z, which was not conducted.

C. AFM pivot measurements

For the hammerhead pivot calibration technique described in this work, basic instrument requirements are a LFM-type (quad-cell PSD) AFM instrument with top-down optics, for viewing the experimental setup, and micro-scale positioning stages for x-y movement of the cantilever relative to the surface, or vice versa. The physical implementation of a hammerhead pivot calibration is depicted in Fig. 6. In Fig. 6(a), a "ramp chip" is mounted on or beside an experimental surface of interest and a selected hammerhead cantilever is installed in the AFM instrument. This cantilever is used to both calibrate the optical lever system (S_N^0, S_T) as well as perform friction-loop measurements (ΔV_L) on the experimental surface. In calibrating S_T, Fig. 6(b) depicts the configuration for a pivot torque-displacement ramp, where the wing of the hammerhead cantilever is in contact with the right dock of the ramp chip at a lever-arm length, H. The probe (out of view on the underside of the cantilever) is positioned at the center of the head, at an effective cantilever length, L^*, from the fixed end of the cantilever. Imposed normal displacement of the ramp chip or cantilever, ΔZ, causes the cantilever to both flex and twist due to the load offset, H.

For the experimental results discussed in this section, force-displacement curves were generated by ΔZ ramping the probe on a flat, featureless area of the ramp chip. Torque-displacement curves were generated by ΔZ ramping on the cantilever wing, as depicted in Fig. 6(b), where fiducial marks on the ramp chip allowed for contact to be established between cantilever and chip at a desired lever-arm length, H, determined readily through the overhead optics of the
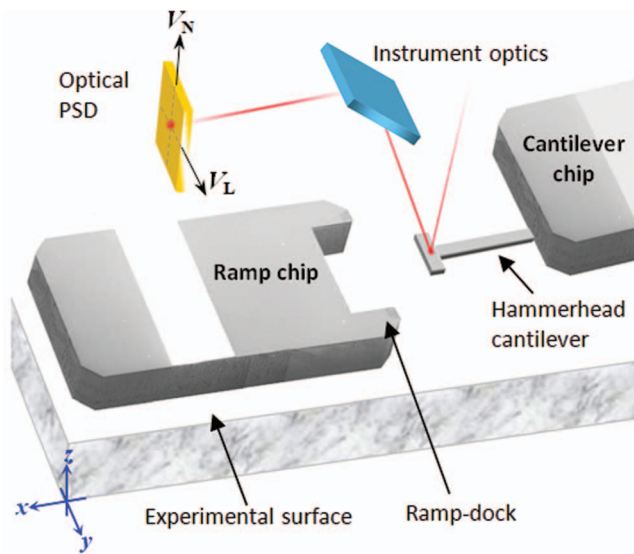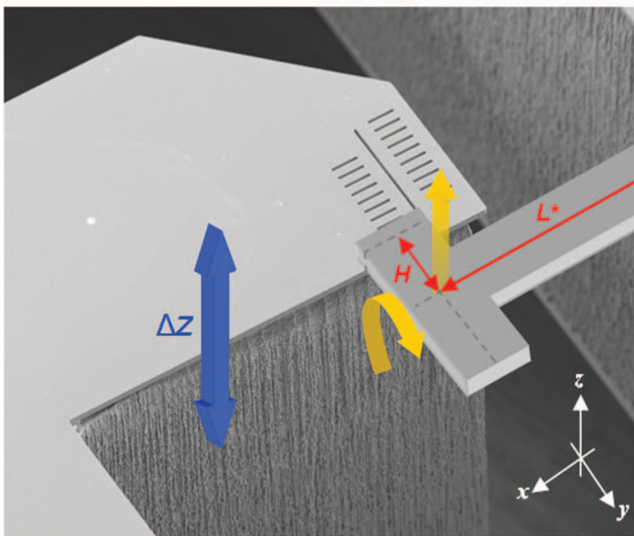
FIG. 6. (Color online) Physical implementation of a hammerhead pivot calibration. (a) An example experimental setup in which a "ramp chip" is mounted on an experimental surface of interest and a selected hammerhead cantilever is installed in the AFM instrument in preparation for a friction experiment. (b) A lever-arm wing of the hammerhead cantilever in contact with the right dock of the ramp chip; the probe (out of view on the underside of the cantilever) is positioned at the center of the head at an effective cantilever length, L^*, from the fixed end of the cantilever; relative displacement of the ramp chip or cantilever in the z-direction, ΔZ, causes the cantilever to both flex and twist due to the load offset, H.

AFM instrument. As a means of establishing "point" contacts between the cantilever and ramp chip, two tungsten spheres were chosen such that they were both $(10 \pm 0.5)\,\mu\text{m}$ in diameter.[22] The spheres were epoxy glued between the chip edge and the first fiducial mark, one on the right dock and one on the left dock, of the ramp chip (not shown).

1. Torque sensitivity calibration

Figure 7 shows torque sensitivity (S_T) pivot calibration plots for two different AFM instrument platforms, "In-
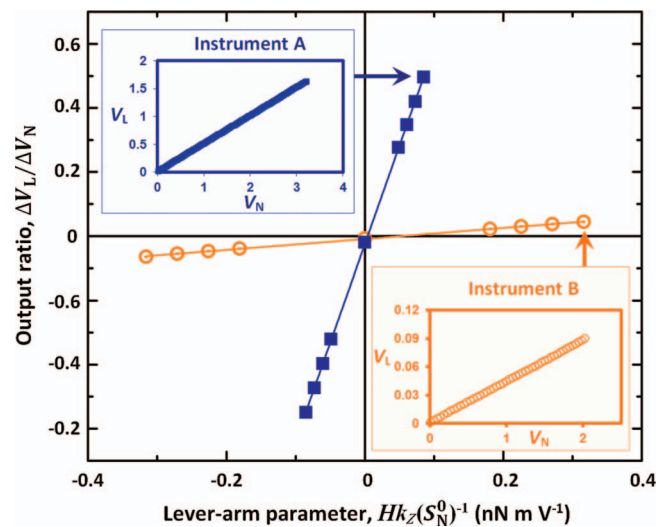

FIG. 7. (Color online) Pivot calibration data collected on two different AFM instruments using the same hammerhead cantilever. The fitted slope of each plot provides the torque sensitivity, S_T, of the respective optical lever system: "Instrument A" (solid squares) and "Instrument B" (open circles). The insets show representative (V_L vs. V_N) pivot data, collected at $H = +70\,\mu\text{m}$ for both instruments. The fitted linear slope of each individual (V_L vs. V_N) observation provides a $\Delta V_L / \Delta V_N$ data contribution to the main plot (the contribution of the inset data is indicated by arrows). Each data point in the main plot represents the average of five such $\Delta V_L / \Delta V_N$ measurements, repeated non-sequentially throughout the calibration for each H lever-arm (x and y uncertainties are smaller than the data points used).

strument A" (solid squares) and "Instrument B" (open circles), using the same hammerhead cantilever as pictured in Fig. 5(b). As suggested by Eq. (8), the output response ratio, $\Delta V_L / \Delta V_N$, is plotted in Fig. 7 against the optical lever-arm parameter, $H k_Z (S_N^0)^{-1}$. The later has three components: k_Z, which was determined in this work by instrumented indentation measurements, described previously (Sec. III B); S_N^0 was determined from force-displacement data obtained during the pivot calibration; and H lever-arm values were also implemented during the pivot calibration. For the experiments described here, the lever-arms used were: $H = 0$; $H > 0$ (i.e., $+40\,\mu\text{m}$, $+50\,\mu\text{m}$, $+60\,\mu\text{m}$, and $+70\,\mu\text{m}$); and $H < 0$ (i.e., $-40\,\mu\text{m}$, $-50\,\mu\text{m}$, $-60\,\mu\text{m}$, and $-70\,\mu\text{m}$); where lever-arm measurement uncertainties were assigned $\pm 2\,\mu\text{m}$, based on the uncertainty of manual H positioning for the AFM instruments used. The insets in Fig. 7 show representative (V_L vs. V_N) pivot data, collected at $H = +70\,\mu\text{m}$ for both instruments. All (V_L vs. V_N) data observed in these experiments were highly linear. The fitted slope of each individual (V_L vs. V_N) observation provides a $\Delta V_L / \Delta V_N$ data contribution to the main plot (the contribution of the inset data is indicated by arrows). Each $H \neq 0$ data point in the main plot represents the mean and standard deviation of five non-sequential repeat torque-displacement measurements (uncertainties for both $\Delta V_L / \Delta V_N$ and $H k_Z (S_N^0)^{-1}$ are smaller than the symbol size shown). Note that data at $H = 0$ are generated by force-displacement loading, which is also used to determine the normal sensitivity, S_N^0, of the optical lever system. The S_N^0 values in Table I represent the mean and standard deviation of 10 non-sequential repeat force-displacement S_N^0 measurements obtained over the course of each calibration for Fig. 7.

From the main plot in Fig. 7 (and Eq. (8)), torque sensitivity, S_T, values for each instrument were calculated as the slope of each plot from least-squares linear fitting.[23] These values are listed in Table I, from which Instrument A is clearly more sensitive to cantilever flex and twist than Instrument B, with S_N^0 values differing by a factor of almost 4 and S_T values differing by more than a factor of 30.

It is apparent in Fig. 7 that S_T calibration plots for both Instruments A and B show a non-zero $\Delta V_L / \Delta V_N$ intercept value at $H = 0$. A non-zero intercept in a S_T calibration plot is caused by system crosstalk. Mechanical crosstalk occurs when an AFM cantilever experiences actual mechanical torque under conditions where torque is supposed to be zero. A common cause of mechanical crosstalk is a probe that is not y-aligned with the shear center of the cantilever, and in the case of a multiple lever-arm pivot S_T calibration, significant mechanical crosstalk would be revealed by nominal zero-torque data ($H = 0$) that fail to form part of a good linear fit with torque ($H \neq 0$) data.[14] Mechanical crosstalk was not observed in experiments conducted here. In many cases, system crosstalk results from optical misalignment—a misalignment between the cantilever reflective (beam bounce) surface and the sector axis of the PSD—which produces a lateral output during flexural deflection of the cantilever, when torque on the cantilever is zero ($H = 0$). In the calibration experiments reported in Fig. 7, optical misalignment produced an Instrument A system crosstalk of $(\Delta V_L / \Delta V_N)_{H=0} = -0.023$, and for Instrument B, $(\Delta V_L / \Delta V_N)_{H=0} = -0.008$. The fact that optical crosstalk is a typical observation in LFM-type optical lever systems suggests that Eq. (8) should be modified to include an intercept term and a perhaps a slope correction for any effect that crosstalk may have on S_T. Discussed further in Sec. V, for optical misalignments that are typically encountered and practically reasonable, crosstalk has only a minimal effect on the measurement of torque sensitivity (less than 1% additional uncertainty in S_T).

2. Cantilever torsional stiffness measurement

The data that provide a torque sensitivity (S_T) calibration of an AFM optical lever system can also be used to determine the torsional stiffness of the cantilever (k_ϕ). A torsional stiffness measurement uses the normal sensitivity parameters, S_N^0 and S_N^H, determined during force-displacement and torque-displacement measurements, respectively (Sec. II B). For the experiments conducted here, Fig. 8 is a plot of the left-hand-side of Eq. (12), $(S_N^0 / S_N^H) - 1$, versus the lever-arm parameter, $H^2 k_Z$. The inverse of the fitted slope is k_ϕ, according to Eq. (12). Figure 8 uses the same symbols scheme as Fig. 7. In the main plot of Fig. 8, each symbol represents the mean and standard deviation of five non-sequential repeat measurements at each of the lever-arms used. The uncertainties in $H^2 k_Z$ are smaller than the symbol size. To provide a basis for comparison between AFM and indenter instrumentation, the flexural stiffness value of the cantilever used for all experimental data was the instrumented indenter determined value of $k_Z = (16.3 \pm 0.1)\,\text{N m}^{-1}$ (Sec. III B). On the Fig. 8 main plot, the solid line represents the torsional stiff-
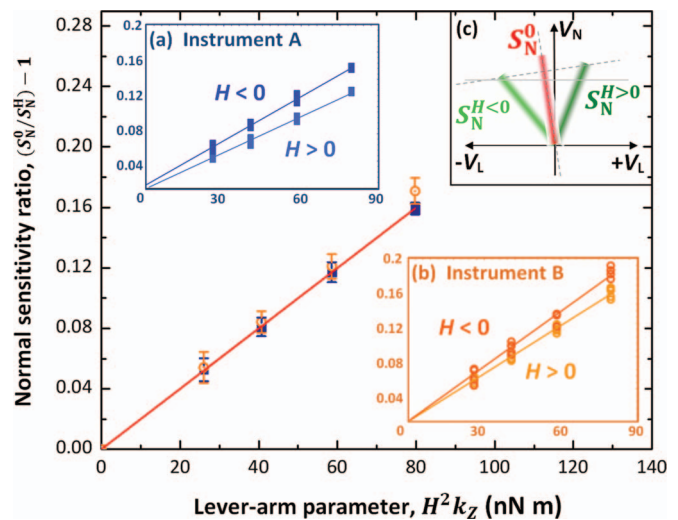

FIG. 8. (Color online) Pivot torsional stiffness measurements of the hammer-head cantilever on two different AFM instrument platforms (same symbols scheme as Fig. 7). The main plot shows averaged data, which is compared to the instrumented indenter value (solid line). All data collected on Instrument A are shown in inset (a); all data collected on Instrument B are shown in inset (b). Inset (c) is an illustrative representation of the optical lever system of both instruments as they were observed here.

ness of the cantilever determined by the instrumented indenter, $k_\phi = (500 \pm 18)\,\text{nN m rad}^{-1}$. Table I lists the cantilever k_ϕ values obtained by all three instruments, which show agreement within two standard errors.

While each data point in the main plot of Fig. 8 represents the mean value of five non-sequential repeat measurements at each of the lever-arms used, the insets show all data collected for Instrument A, in Fig. 8(a), and all data for Instrument B, in Fig. 8(b). The inset plots reveal systematic deviations in the determination of $(S_N^0 / S_N^H) - 1$, which tend to increase with increasing H. In fact, the system response is split according to $H > 0$ and $H < 0$ lever-arms for both instruments. The splitting effect is due to crosstalk caused by the optical misalignment described above. (Again, note that the example data shown in Fig. 3 were acquired especially to demonstrate the basic principles of the pivot calibration technique using a well-aligned optical lever system; the Fig. 3 data are not related to data shown in Figs. 7 and 8.) To illustrate the misalignment that was present in both instruments A and B, inset Fig. 8(c) depicts the upper two quadrants of a PSD, along with conceptual lines that represent laser spot movement during cantilever loading for: $H = 0$ force-displacement loading, generating S_N^0 (center); $H > 0$ torque-displacement loading, generating $S_N^{H>0}$ (right); and $H < 0$ torque-displacement loading, generating $S_N^{H<0}$ (left). The configuration shown in Fig. 8(c) is representative of the state of both AFM instruments as they happened to be set up for these experiments, such that the order of normal sensitivities was found to be $S_N^0 > S_N^{H>0} > S_N^{H<0}$. In other words, the optical crosstalk caused and perpetuated the difference $(S_N^0 / S_N^{H>0}) - 1 < (S_N^0 / S_N^{H<0}) - 1$, which became progressively greater with larger cantilever twist (i.e., larger H). In the case of each instrument, a k_ϕ value was obtained by applying a least-squares linear fit to all data[23] (see Sec. V for

more discussion on this fitting approach), which gave inverse slopes of $k_\phi = (503 \pm 17)\,\mathrm{nN\,m\,rad}^{-1}$ for Instrument A and $k_\phi = (471 \pm 10)\,\mathrm{nN\,m\,rad}^{-1}$ for Instrument B. These values are listed in Table I.

IV. ANALYSIS OF HAMMERHEAD CANTILEVER MECHANICS

In Sec. III of this paper, the hammerhead pivot method was examined experimentally, with a focus on *precision* in calibrating the torque sensitivity (S_T) of AFM optical lever systems, via Eq. (8). In this section, the potential *accuracy* of the pivot method is investigated by way of mechanical simulation.

The accuracy of the pivot torque sensitivity method relies on the simultaneous validity of Eqs. (2), (3), (6), and (8), where Eqs. (3) and (6) describe how the cantilever is used as an optical lever force transducer, and Eqs. (2) and (8) are used to calibrate the AFM optical lever sensitivities, S_N^0 and S_T, respectively. When used as a force transducer, the cantilever is loaded at the probe apex. During a pivot calibration, the hammerhead cantilever is loaded on the wings as well as on the probe. While relating one load configuration to another in this way is supported by beam theories for flexure and torsion, the accuracy of these theories is limited by the simplifying assumptions that were used to derive them. In the light of the precision demonstrated by experimental measurements in Sec. III (i.e., <1 % statistical uncertainty), this section describes the use of three-dimensional continuum elasticity theory, implemented via the finite element method,[25] to estimate the magnitude of possible systematic errors resulting from simplifying assumptions about the cantilever mechanics implicit in the hammerhead pivot calibration method.

In the following, Sec. IV A discusses the properties of the cantilever model, the application of simulated loads to the model and analysis of its response, as well as analysis of simulation measurement errors. Analysis of the hammerhead cantilever mechanics involved simulating the experiments described in previous sections of this paper. In Sec. IV B, simulated instrumented indentation loading is discussed—analogous to experiments in Sec. III B. In Sec. IV C, simulated AFM pivot loading is examined—analogous to experiments in Sec. III C—in terms of its potential to accurately calibrate lateral forces. Section IV D examines the approximation that, during lateral loading at the apex of the probe, the shear center of the cantilever is located at the centroid of its rectangular cross-section, along the entire cantilever length (*x*-axis), such that the moment lever-arm, *h*, can be determined from the distance between the centroid and the load point.

A. Simulation methods

The prototype hammerhead cantilever model was generated and analyzed using commercial software. The following describes the simulation procedure in terms of the physical properties of the model, the application of loads and analysis of response, as well as analysis of errors in relation to a (simulated) pivot calibration.
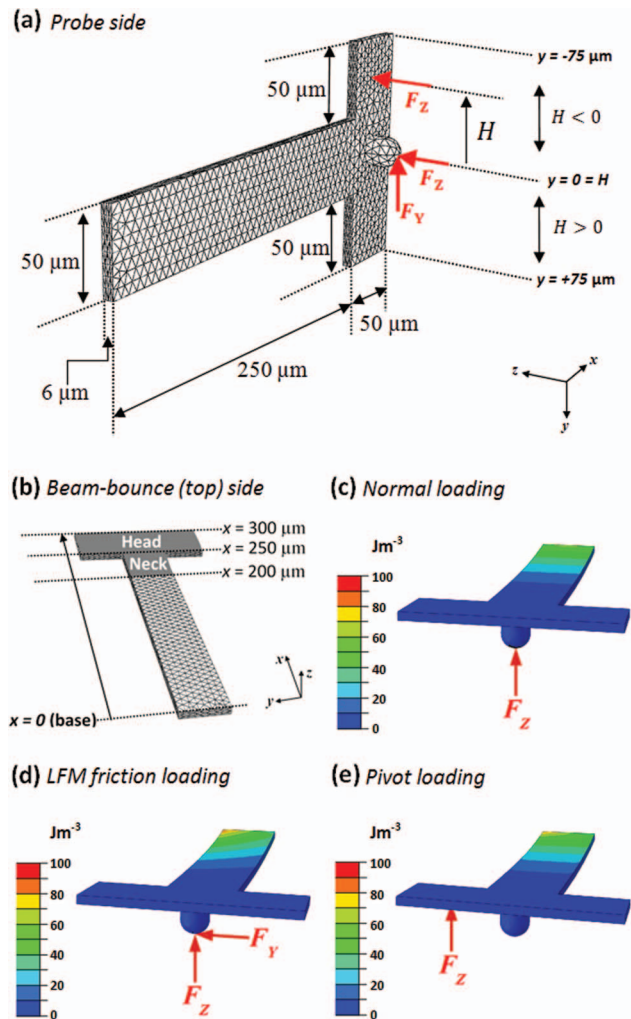

FIG. 9. (Color online) Finite element model of hammerhead cantilever (medium mesh). (a) Cantilever dimensions and typical forces applied to the probe side of the cantilever. (b) The beam-bounce side of the cantilever, along with the shaded "head" region (and "neck" region), used to determine angular deflection responses of the cantilever. (c)-(e) Simulated deformed cantilevers in response to 5 μN loads, in which displacements are magnified 100 times and contours indicate elastic strain energy density; the lever-arm used in (e) is $H = 40\,\mu$m.

1. Cantilever model properties

Representative illustrations of the hammerhead cantilever model are shown in Fig. 9, where Fig. 9(a) is the "probe side" of the cantilever model with dimensions and loads relevant to pivot and lateral loading. Fig. 9(b) shows the "beam bounce side" of the cantilever (opposite side to probe), showing two regions that were used to observe the flexural, θ, and torsional, ϕ, angular deflection responses of the cantilever: the $50\,\mu$m $\times$ $150\,\mu$m "head" region and the $50\,\mu$m $\times$ $50\,\mu$m "neck" region. While the majority of analysis used the head region to calculate cantilever deflection, a later analysis in Sec. IV C 2 compares the deflection response of the cantilever across the head versus across the neck.

Silicon elastic constants used for the cantilever material were:[24] $c_{11} = 165.77$ GPa, $c_{12} = 63.924$ GPa, and $c_{44} = 79.619$ GPa. The x–y-plane of the cantilever was the {100} plane and the longitudinal axis of the cantilever (*x*-direction)

was a $\langle 110 \rangle$ direction. Outlined in Appendix A, the model consisted of 10-node quadratic tetrahedrons, and a sequence of three mesh densities was used to generate estimated values and numerical errors. The dimensions of the model, shown in Fig. 9, correspond to the nominal dimensions of the microfabricated cantilevers used in experiment: $300\,\mu\text{m}$ long (x-dimension), $50\,\mu\text{m}$ wide (y-dimension) and $6\,\mu\text{m}$ thick (z-dimension). The cantilever probe is located at $x = 275\,\mu\text{m}$ from the base and at $y = 0$ in the center of the head. The probe was modeled as a cylinder with a $10\,\mu\text{m}$ radius, terminating in a hemispherical cap of $10\,\mu\text{m}$ radius; the total height of the probe, with cap, was $20\,\mu\text{m}$ (Fig. 9(a)). The probe lever-arm length was thus $h = 23\,\mu\text{m}$, which incorporates the probe length (from the base of the cylinder to the apex of the cap) and half the thickness of the cantilever. No attempt was made to exactly reproduce the dimensions and material properties specific to the cantilever used in experiments, not least because properties such as thickness and uniformity are difficult to ascertain, and furthermore, the fixed-end boundary conditions used in the model were set as fully constrained, which neglects the actual boundary conditions that would exist in the area where the cantilever meets the handling chip, particularly considering the undercut shelf present on microfabricated cantilevers used in this work (see Fig. 4(b)). A more realistic boundary condition, for the region where the base of the cantilever meets the handling chip, was not specifically investigated in this work.

2. Load and response modeling

For all modeling analysis carried out here, simulated forces applied to the cantilever model were $5\,\mu\text{N}$, which represents a typical large (about maximum) load used in experiments. The applied forces were approximated as point forces, a convenient simplification in numerical modeling when, as in the experiments here (Sec. III B), contact compliance can be neglected (Appendix A). To illustrate the distribution of elastic deformation in the cantilever during each of the three load configurations relevant to this work, Figs. 9(c)–9(e) show elastic strain energy density profiles for: F_Z on the probe (normal loading), in (c); F_Z and F_Y applied simultaneously on the probe (lateral friction loading), in (d); and, F_Z in pivot loading on the wing at a lever-arm distance $H = 40\,\mu\text{m}$, in (e). Note that Figs. 9(d) and 9(e) show similar energy density distributions for LFM friction loading and pivot loading, respectively.

Analysis of the hammerhead cantilever mechanics involved simulating the experiments described in previous sections of this paper. Analogous to instrumented indentation experiments (Sec. III B), the results of simulated indentation loading are summarized in Sec. IV B below, and described in greater detail in Appendix B. In order to simulate AFM pivot loading experiments (Sec. III C), the results of cantilever head rotations in response to applied (pivot) loads are summarized in Sec. IV C below. To provide a basis for AFM pivot loading analysis, the optical lever sensitivity and force transduction equations that are central to an AFM pivot calibration—Eqs. (2), (3), (6), and (8)—were "conceptually transferred" from the AFM optical lever system domain to the mechan-

ical domain of the finite element model by assuming the gains of both normal and lateral quad-cell PSD sectors to be $1\,\text{V}\,\text{rad}^{-1}$. In this case, expressions for cantilever force, $F_Z = k_Z \Delta Z = k_\theta \theta$, and torque, $T = k_\phi \phi$, (Sec. II A) were then subjected to the substitutions, $\Delta V_\text{N} \rightarrow \theta$ and $\Delta V_\text{L} \rightarrow \phi$, respectively, giving $S_\text{N}^0 \rightarrow k_\theta^{-1} k_Z$ and $S_\text{T} \rightarrow k_\phi^{-1}$, respectively. Using these substitutions, Eqs. (2), (3), (6) and (8) become

$$\theta = k_\theta^{-1} (F_Z)_I \,, \tag{2'}$$

$$(F_Z)_O = k_\theta \theta, \tag{3'}$$

$$(F_Y)_O = (k_\phi / h)\phi, \tag{6'}$$

$$\frac{\phi}{\theta} = \left(\frac{k_\theta}{k_\phi}\right) H. \tag{8'}$$

The above equations are referred to henceforth as the "calibration equations"; the subscript $()_I$ indicates input forces, which are forces applied directly to the cantilever; the subscript $()_O$ indicates output forces, which are the forces determined via simulated calibration. Cantilever rotations, θ and ϕ, were calculated using the small-angle formulas applied to the average surface gradients of the "head" region of the hammerhead cantilever (Fig. 9(b)), such that

$$\theta = \overline{\partial z'/\partial x} = -\frac{A_x}{A_z}, \quad \phi = -\overline{\partial z'/\partial y} = \frac{A_y}{A_z},$$

$$\text{with } \vec{A} = \oint \vec{r} \times \overrightarrow{dl} \,, \tag{13}$$

where z' is the vertical position of the deformed top surface of the head (as a function of x and y), and the contour integral is taken over the boundary of the top surface of the head.

3. Estimation of errors

In performing simulations, physical quantities (such as forces and displacements) were obtained via analysis of three mesh densities of the cantilever model. Outlined in Appendix A, the results for each model were obtained and then trends in numerical results were analyzed using the Richardson extrapolation method[26] to obtain the best estimate for the physical quantity and associated numerical error, reported in the form $(A \pm B)$, where A is the best estimator of the quantity and B is the numerical error in that estimator.

The quantities of interest in the simulation study were the system calibration parameters and the interpretation of forces via those calibration parameters, both generated by methods analogous to experimental procedure. In the mechanical domain of the numerical simulation, the calibration parameters that are analogous to S_N^0 and S_T are actually cantilever stiffness and compliance parameters, $k_Z k_\theta^{-1}$ and k_ϕ^{-1}, respectively. Systematic errors in these parameters were determined by comparing them against "reference values," which are listed in Table II as cantilever stiffness values, $(k)_\text{exact}$, and compliances, $(k^{-1})_\text{exact}$. For all practical purposes in this work, the reference values were assumed to carry zero systematic error into the calculation of calibration parameters and forces. The reference value $(k_Z)_\text{exact}$ was

TABLE II. Reference values for simulated hammerhead cantilever.

Load (5 μN)	Displacement			Equation used	Calculated reference values (stiffness and compliance)
	ΔZ (nm)	θ (mrad) Eq. (13)	ϕ (μrad) Eq. (13)		
$(F_Z)_I = 5\,\mu\text{N} = (F_Z)_O$	227.50 ± 0.05	1.2380 ± 0.0002	N.A.	Eq. (1)	$(k_Z)_{\text{exact}} = (21.978 \pm 0.005)\,\text{N m}^{-1}$
					$(k_Z^{-1})_{\text{exact}} = (45.50 \pm 0.01)\,\text{mm N}^{-1}$
				Eq. (3′)	$(k_\theta)_{\text{exact}} = (4.0387 \pm 0.0006)\,\text{mN rad}^{-1}$
					$(k_\theta^{-1})_{\text{exact}} = (247.60 \pm 0.04)\,\text{rad N}^{-1}$
$(\vec{F})_I = (5\hat{y} + 5\hat{z})\mu\text{N} = (\vec{F})_O$	227.49 ± 0.05	1.2380 ± 0.0002	162.05 ± 0.08	Eq. (6′), $h = 23\,\mu\text{m}$	$(k_\phi)_{\text{exact}} = (709.67 \pm 0.13)\,\text{nN m rad}^{-1}$
					$(k_\phi^{-1})_{\text{exact}} = (1.4091 \pm 0.0007)\,\text{rad}\,(\mu\text{N m})^{-1}$

defined from Eq. (1) using an input load of $(F_Z)_I = 5\,\mu\text{N}$, applied to the probe of the cantilever model, with ΔZ determined from the point-load displacement. From the same applied load, Eq. (3′) was used to define $(k_\theta)_{\text{exact}}$ by setting the output load equal to the input load, $(F_Z)_O = (F_Z)_I = 5\,\mu\text{N}$, and using Eq. (13) to determine θ. By applying a compound load, $(\vec{F})_I = (5\hat{y} + 5\hat{z})\,\mu\text{N}$, to the cantilever probe, and using Eq. (13) to calculate ϕ, $(k_\phi)_{\text{exact}}$ was calculated using $h = 23\,\mu\text{m}$ and by setting $(F_Y)_I = (F_Y)_O = 5\,\mu\text{N}$ in Eq. (6′). From Table II, which lists the calculated reference values and relevant displacements, note that good agreement between $(F_Z)_I$ and $(\vec{F})_I$ (in both θ and ΔZ) indicates that flexural deflection is independent of torque, as suggested by a linear superposition of the twist and flex deformations.

The calibration parameter reference values in Table II were used to calculate systematic errors in simulated pivot calibration parameters, k^{-1}, such that

$$\left| \frac{\Delta k^{-1}}{k^{-1}} \right| = \frac{|k^{-1} - (k^{-1})_{\text{exact}}|}{|(k^{-1})_{\text{exact}}|}, \qquad (14)$$

Simulated output forces, $(F)_O$, are calculated via the calibration equations above, where systematic error in a given force value is calculated by comparing it to a respective input force, $(F)_I$, such that

$$\left| \frac{\Delta F}{F} \right| = \frac{|(F)_O - (F)_I|}{|(F)_I|}. \qquad (15)$$

Results for both Eq. (14) and Eq. (15) are reported as percentages in the form $(C \pm D)\,\%$, where C is the simulated systematic error and D is the numerical error associated with this error value.

Finally, as beam flexure and torsion theories are linear (small-deformation) theories, Eqs. (2), (3), (6), and (8) are only valid for the small-load limit. Systematic error due to non-linear behavior was investigated with additional modeling (not reported in detail), which revealed that geometric nonlinearity—including torsional and flexural deformation coupling—had a negligible effect for all forces and moment arms of interest here.

4. Localized deformation

In experiment, loads are applied to the hammerhead cantilever by pressing the wings against a probe on a ramp chip or cantilever probe against a surface. In simulation, the effect of localized loading is depicted in Figs. 10(a) and 10(b) in which mechanical responses to localized loads are compared with uniformly distributed statically equivalent loads applied to the cantilever. Figure 10(a) shows the cantilever deformation response to a pivot point-load, $F_Z = 5\,\mu\text{N}$, applied to the cantilever with an eccentricity, $H = 40\,\mu\text{m}$ (on the left-hand wing). Figure 10(b) shows the cantilever response to point-loading, $\vec{F} = -5y + 5z\,\mu\text{N}$, applied at the probe apex ($h = 23\,\mu\text{m}$), where F_Y is directed toward the left of the picture. Figures 10(a) and 10(b) also show the cantilever deformation response to uniform body forces (same resultant) applied to the cantilever head region (Fig. 9(b)), where a rotational force, centered around the x-axis, was applied to give the same couple as the point force. Although the point force and distributed body forces are statically equivalent, and therefore cause nearly identical global mechanical responses, Fig. 10 reveals small differences in the deformation response for each loading case. In both Figs. 10(a) and 10(b), the original undeformed shape of the cantilever is shown as medium coarse mesh; the outlines represent the displacement response to distributed body forces, $\vec{u}_{\text{uniform}}$, with displacements exaggerated 100 times (i.e., $\vec{u}_{\text{outline}} = 100 \times \vec{u}_{\text{uniform}}$); the overlaid contoured surface is the z-component of the displacement difference between the point-load displacement, $\vec{u}_{\text{point}}$, and displacement due to the uniformly distributed force, $\vec{u}_{\text{uniform}}$, exaggerated an additional 200 times (i.e., $\vec{u}_{\text{surface}} = 100 \times \{\vec{u}_{\text{uniform}} + 200 \times [\vec{u}_{\text{point}} - \vec{u}_{\text{uniform}}]\}$).

In Fig. 10(a), where $H = 40\,\mu\text{m}$, the maximum wing flexure displacement was $z \approx 750$ picometers. In the case of $H = 70\,\mu\text{m}$ (not shown), maximum wing flexure was about $z \approx 2.6$ nm. In Fig. 10(b), the maximum head deformation was about $z \approx 112$ picometers, localized in a region that is offset from the probe in the direction of the lateral load. These relatively small head deformations turn out to be important for the analysis of cantilever response in simulations of both indentation and AFM pivot loading in Secs. IV B–IV C.

B. Indenter simulations

For a series of lever-arm positions, H, across the head of the cantilever model, $5\,\mu\text{N}$ loads were applied and displacement, ΔZ, at the point of force application was used to determine compliance as a function of H. Analogous to experiment in Sec. III B, least-squares fitting to Eq. (10) was then performed for each mesh resolution to
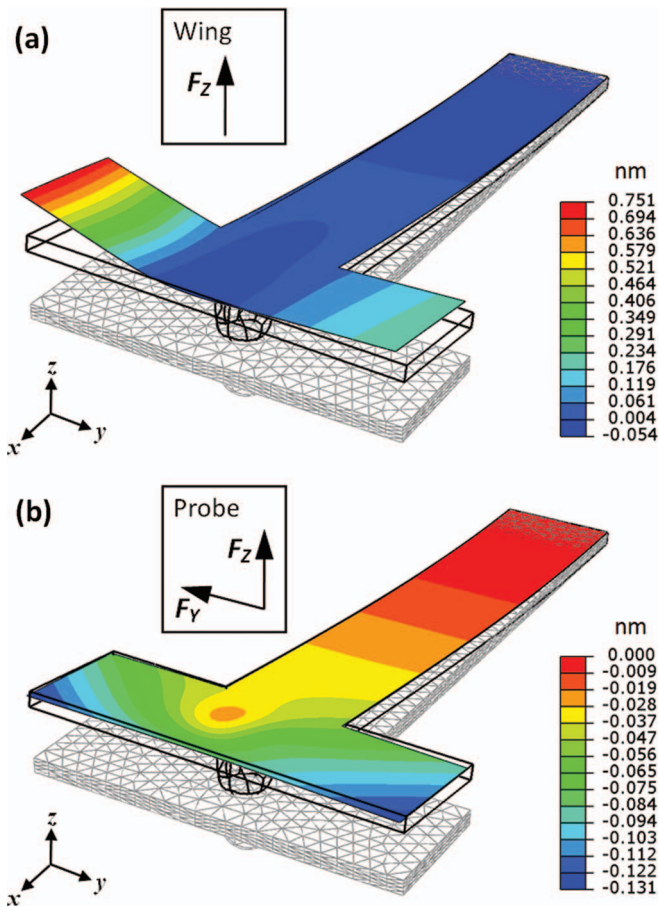
FIG. 10. (Color online) Hammerhead cantilever subjected to 5 μN loads. (a) Normal load, F_Z, applied at $H = 40 \, \mu$m on the wing. (b) Simultaneous normal (F_Z) and lateral (F_Y) load applied at the probe apex. Both (a) and (b) show relative mechanical displacement responses of the cantilever model. The medium meshes are the original undeformed cantilever shapes. The outlines represent the displacement response to distributed body forces, $\vec{u}_{\text{uniform}}$, with displacements exaggerated 100 times ($\vec{u}_{\text{outline}} = 100 \times \vec{u}_{\text{uniform}}$). The overlaid contoured surface is the z-component of the displacement difference between displacement of a point-load, $\vec{u}_{\text{point}}$, and that due to a uniformly distributed force, $\vec{u}_{\text{uniform}}$, exaggerated an additional 200 times ($\vec{u}_{\text{surface}} = 100 \times \{\vec{u}_{\text{uniform}} + 200 \times [\vec{u}_{\text{point}} - \vec{u}_{\text{uniform}}]\}$).

trast to the quantification of k_Z, the explicit quantification of k_ϕ is not required for a pivot determination of S_T, and thus for the calibration of LFM lateral friction forces. However, the relatively large error associated with the simulated indenter k_ϕ value highlights a possible shortcoming in assumptions underlying the mechanical response of the cantilever to indentation loading: notably the completeness of Eq. (10).

The head deformation illustrated in Fig. 10(a) is largely due to flexure of the "wings" of the hammerhead cantilever during ΔZ (pivot) loading. This is demonstrated in Appendix B, which describes a modification of Eq. (10) to include a wing flexure term. Results of this analysis are also summarized in Table III. For the current hammerhead cantilever design, the key findings of the Appendix B simulation analysis are that the measurement of flexural stiffness at L^* can be determined with errors of $< 1\%$ using multiple instrumented indentation measurements across the head of the hammerhead cantilever (multiple H values at L^*), as done experimentally, without the need to account for wing flexure in the measurement model. On the other hand, if a torsional stiffness measurement is required, the simulation study predicts that wing flexure must be accounted for in any model used to fit indentation force-displacement data if measurement errors are to be kept to a percent-level or less.

C. AFM pivot simulations

For an optical lever system that is calibrated for LFM friction measurements via the hammerhead pivot calibration method, the accuracy of friction measurements are strongly dependent on the accuracy of the pivot determined torque sensitivity of the optical lever system (S_T). This section examines the potential of the current hammerhead cantilever design to accurately determine S_T, and furthermore, to facilitate an accurate measurement of normal and lateral (friction) surface forces.

1. Accuracy potential of hammerhead torque sensitivity calibration

For the hammerhead cantilever design used in this work, three key aspects of the hammerhead pivot calibration method were examined with regard to accuracy: (1) The transduction of force and torque applied to the cantilever via F_Z pivot loading; (2) The determination of torque sensitivity, S_T, from the ratio of cantilever torsional (twist) to flexural (rotation)

give stiffness values for k_Z and k_ϕ. Finally the best estimate and uncertainty errors were determined using Richardson extrapolation (Appendix A). The flexural stiffness determined from this analysis was $k_Z = (22.013 \pm 0.005) \, \text{N m}^{-1}$, which agreed to within 0.2% of the $(k_Z)_{\text{exact}}$ reference value (Table II). The respective torsional stiffness value was $k_\phi = (664.5 \pm 0.1) \, \text{nN m rad}^{-1}$, which compared only to within 7% of its reference value (Table II). In con-

TABLE III. Modeled normal and torsional stiffness values for simulated indentation of hammerhead cantilever. See Appendix B for analysis.

	Without wing flexure: Eq. (10) or Eq. (B2) with $a = 0$	With wing flexure: Eq. (B2) with $a = 1$	With wing flexure: Eq. (B2) with $a_{\text{fit}} = 0.84 \pm 0.03$	Reference value
Flexural stiffness k_Z, (N m^{-1})	22.013 ± 0.005	21.979 ± 0.005	21.985 ± 0.005	21.978 ± 0.005
Fractional error in k_Z, $\frac{|k_Z - (k_Z)_{\text{exact}}|}{(k_Z)_{\text{exact}}}$ (%)	0.1606 ± 0.0002	0.0056 ± 0.0002	0.0313 ± 0.0002	0
Torsional stiffness, k_ϕ (nN m rad^{-1})	664.5 ± 0.1	705.0 ± 0.1	697.9 ± 0.2	709.7 ± 0.1
Fractional error in k_ϕ, $\frac{|k_\phi - (k_\phi)_{\text{exact}}|}{(k_\phi)_{\text{exact}}}$ (%)	6.37 ± 0.01	0.6563 ± 0.0003	1.65 ± 0.02	0

responses during pivot loading for a range of torque lever-arms, H; and (3) The use of S_T in quantifying F_Y lateral forces applied to the probe. To carry out the pivot calibration study, input loads of $(F_Z)_I = 5\,\mu$N were applied at lever-arm distances $H = (40, 50, 60,$ and $70)\,\mu$m, analogous to experiment, and Eq. (13) was used to analyze the cantilever response in terms of rotation, θ, and twist, ϕ, of the head.

To address issue (1), flexural rotation, θ, of the cantilever head was calculated via Eq. (13) for each applied load at each value of H. Taking the stiffness of the cantilever to be $k_\theta^{-1} = (k_\theta^{-1})_{\text{exact}}$ in Eq. (3'), excellent agreement was found between $(F_Z)_I = 5\,\mu$N input values and the calculated $(F_Z)_O$ output values for all H, with the largest discrepancy found for the longest moment lever-arm, $H = 70\,\mu$m, which had a relative error of $|\Delta F_Z/F_Z| = (0.09 \pm 0.01)\,\%$ (Eq. (15)). As force enters into the pivot calibration by way of flexural deflection of the cantilever, this small estimated error demonstrates that the metrology underpinning the pivot calibration method is sound in terms of the quantification of force and torque applied to the hammerhead cantilever by pivot loading.

To address issue (2), calculated ϕ/θ values (Eq. (13)) were plotted as a function of $k_\theta H$, as suggested by Eq. (8'), and setting $k_\theta = (k_\theta)_{\text{exact}}$ (Table II). The slope of the plot (not shown) gave $(k_\phi^{-1})_{S_T} = (1.4425 \pm 0.0006)\,\text{rad}\,(\mu\text{N m})^{-1}$; where $(k_\phi^{-1})_{S_T}$ is denoted with a torque sensitivity (S_T) subscript to indicate that it was calculated in a way analogous to the experimental S_T (Eq. (8)). The systematic error in this simulated pivot calibration parameter was determined by comparison with the reference value for the cantilever torsional compliance, $(k_\phi^{-1})_{\text{exact}}$ (Table II) via Eq. (14), which gave $|\Delta(k_\phi^{-1})_{S_T}/(k_\phi^{-1})| = (2.369 \pm 0.009)\%$.

In addressing issue (3), just as S_T is used to calibrate lateral force measurements experimentally, via Eq. (6), the analogous simulation value, $(k_\phi^{-1})_{S_T}$, was used to calibrate lateral force, via Eq. (6'). Listed in Table II, a load of $(\vec{F})_I = (5\hat{y} + 5\hat{z})\,\mu$N, applied to the probe apex, resulted in head rotations, $\theta = (1.2380 \pm 0.0002)\,\text{mrad}$ and $\phi = (162.05 \pm 0.08)\,\mu\text{rad}$. Using the simulated torque sensitivity parameter, $(k_\phi^{-1})_{S_T} = (1.4425 \pm 0.0006)\,\text{rad}\,(\mu\text{N m})^{-1}$, calculated above from Eq. (8'), as well as $h = 23\,\mu$m, and $\phi = (162.05 \pm 0.08)\,\mu\text{rad}$, the lateral applied load was calculated from Eq. (6') to be $(F_Y)_O = (4.8843 \pm 0.0004)\,\mu$N, where systematic error was calculated from Eq. (15) to be

$$|\Delta F_Y/F_Y| = |(F_Y)_O - (F_Y)_I|/|(F_Y)_I|$$
$$= |[[(k_\phi^{-1})_{S_T}]/h]\phi - (F_Y)_I|/|(F_Y)_I|$$
$$= (2.313 \pm 0.008)\,\%.$$

In summary, the finite element simulation study of hammerhead pivot accuracy for the current cantilever design predicts errors on the order of 2\% to 3\% in the determination of optical lever torque sensitivity (S_T), which carry through to result in errors of the same magnitude in the measurement of lateral (friction) forces. A reduction of error in S_T will thus reduce errors in LFM friction force measurement. The following Sec. IV C 2 explores ways to reduce such error by reducing or avoiding the major contributor to it.

2. Hammerhead head deformation error

The above simulation study demonstrated errors of approximately 2\% in the determination of a simulated torque sensitivity pivot calibration parameter, $(k_\phi^{-1})_{S_T}$, and transduced lateral force, F_Y. The indenter simulation study, outlined in Sec. IV B (detailed in Appendix B; Table III), revealed errors on the order of about 6\% in the measurement of k_ϕ, caused by small deformations in the head of the cantilever during loading (i.e., when head deformation was not accounted for). From Fig. 10(a), the effect of such deformation is to generate asymmetric wing shapes, sufficient to alter the average slope of the head, such that the apparent twist angle ($\phi = \overline{\partial z'/\partial y}$) is not a unique function of torque. While the extent to which such deformation will translate to actual errors in the AFM optical lever response (for different spot sizes and shapes) is currently unknown, the simulation technique that was used to identify small head deformation also elucidates possible ways to reduce it or avoid errors that could result from it. Three considerations are discussed: (1) utilizing St. Venant's principal in reading the angular response of the loaded cantilever; (2) better characterization and use of the relationship between lever-arm length and head deformation arising from wing flexure; and (3) optimizing future cantilever design.

In regard to approach (1), the success of beam bending and torsion theory is attributable in large part to St. Venant's principal,[15] by which the local effects of forces can be ignored, provided they are analyzed far enough away. The local head deformation, discussed previously and illustrated in Figs. 10(a) and 10(b), suggests that deformations near the points of force application are important, and consequently the details of force position matter. One possible approach to reduce systematic error is therefore to render these local deformations as "less important" by measuring cantilever rotations closer to the fixed-end base of the cantilever (further away from the load application region). Fig. 9(b) shows a $(50 \times 50)\,\mu\text{m}^2$ region marked "neck," adjacent to the head region of the cantilever. Using the same forces and analysis as used previously, but analyzing θ and ϕ by applying Eq. (13) to the neck region, the estimated systematic method error for lateral force was $|\Delta F_Y/F_Y| = (0.33 \pm 0.03)\,\%$, compared with $(2.313 \pm 0.008)\,\%$ from the same analysis on the head region. By observing θ and ϕ rotations in the neck region, which are caused by strains along the cantilever between the fixed base and the neck region, the irregular strains closest to the point loads in the head region do not contribute significantly to the overall rotations. The theoretical exercise conducted here therefore suggests that experimental force transduction accuracy could be improved if the AFM laser spot is positioned on the "neck" of the cantilever rather than on the "head."

Approach (2) is to reduce wing flexure by using shorter lever-arms for pivot loading—a reduced lever-arm meaning a stiffer wing for the same applied load. To investigate this possibility, individual simulation torque sensitivity values were found for each value of H, such that $(k_\phi^{-1})_H = k_\theta^{-1}\phi/H\theta$, rather than using the slope of Eq. (8') as done in Sec. IV C 1. Relative systematic error for each of these
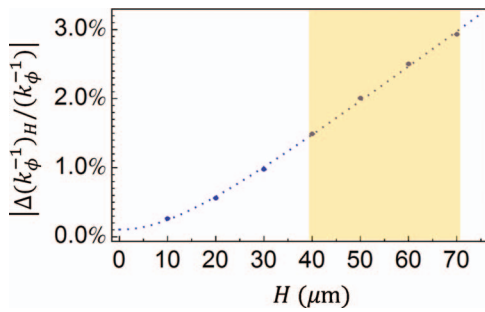
FIG. 11. (Color online) Systematic error, $|\Delta(k_\phi^{-1})_H/(k_\phi^{-1})|$, in torsional compliance versus load eccentricity, H.

individual values were calculated as

$$\left|\frac{\Delta(k_\phi^{-1})_H}{(k_\phi^{-1})}\right| = \frac{\left|\frac{(k_\theta^{-1})_H \phi}{H\theta} - (k_\phi^{-1})_{\text{exact}}\right|}{|(k_\phi^{-1})_{\text{exact}}|}. \qquad (16)$$

Figure 11 is a plot of $|\Delta(k_\phi^{-1})_H/(k_\phi^{-1})|$ *vs. H*, in which systematic errors reduce from about 3 % for $H = 70\,\mu$m to less than 1 % for lever-arms of $H = 30\,\mu$m or less. The shaded area in Fig. 11 indicates H values used in experiments (i.e., $H = 40\,\mu$m to $70\,\mu$m).

A possible third approach would be to reduce head deformation by cantilever design. For example, a cantilever with a head that is thicker (larger z-dimension) than the rest of the cantilever body would have a larger wing stiffness, which would reduce wing flexure during pivot loading. In future cantilever designs and method development, it would be advisable to consider all three of the solutions proposed here.

D. Center of shear

The discussion so far has assumed that the appropriate origin for determining torque (known as the center of shear[15]) is the centroid of the cantilever rectangular cross-section. In this way, the moment lever-arm, h, can be determined from the distance from the centroid to the load point. Strictly speaking, this is not the case for lateral loads applied at the probe, and additional finite element modeling was performed to determine how much of the previously analyzed systematic error in simulated lateral force calibration could be due to adopting the simplifying assumption of a non-eccentric center of shear.

The shear center of the cantilever is coincident with the centroid of the y–z-plane cross-section for most of the cantilever's length (x-values). However, for values of x where this cross-section cuts through the probe, the y–z-plane cross-section is not symmetric about the x–y-plane, and both the centroid and the shear center in these planes shift along the z-axis and by different amounts. Note that the varying center of shear means that the resisting torque is not constant along the entire length of the cantilever. To examine the problem, a condition of "zero nominal moment arm" was simulated by applying a force, $\vec{F} = F_Y\hat{y}$, with a line of action through the nominal centroid of the cantilever head, at $x = 275\,\mu$m, $y = -75\,\mu$m and vertical (z) position $3\,\mu$m below the top surface (Fig. 9). Under this load, if the nominal centroid and shear center do not coincide, then the cantilever will twist,

giving an effective weighting of the torque along the entire cantilever, $\phi_s = \int \frac{T(x)}{[G(x)J(x)]}dx$, where T is torque, G is shear modulus, and J is the appropriate geometrical factor (similar to a polar moment used to analyze torsion of circular shafts[27]). In this case, an average eccentricity of the center of shear along the z-axis, for all x, $\overline{\delta_h} = (k_\phi\phi_s/F_Y)$, can be defined as the residual moment arm when the nominal moment arm is zero. Following similar modeling procedures to those described earlier, and using Richardson extrapolation (Appendix A), the estimated average eccentricity of the center of shear was found to be $\overline{\delta_h} = (11.2 \pm 0.9)$ nm. When compared with the value of $h = 23\,\mu$m, the systematic error is less than (0.049 ± 0.004) %. This result is not surprising, as the nominal center of shear coincides with the cross-section centroid of the cantilever for the majority of the cantilever length, where the majority of twisting takes place (only a small portion of the cantilever length near the probe contributes to the offset). This error was taken into account implicitly in systematic error estimates in Sec. IV C (not listed as an additional error contribution).

V. DISCUSSION

The microfabricated hammerhead cantilevers presented here facilitate a practical and straight-forward means to deliver precise AFM optical lever system calibrations for cantilever flexure (by normal forces) and twist (by friction forces) that can be carried out *in situ* in conjunction with force measurements. The study conducted here demonstrated the use of a hammerhead cantilever under pivot loading to generate optical lever torque sensitivity (S_T) calibrations with sub-percent relative uncertainties on two different AFM instruments (≈ 0.2 % for Instrument A and ≈ 0.6 % for Instrument B; see Table I). This is a significant reduction from the several percent achieved with pivot calibrations on rectangular commercial cantilevers, which required an AFM instrument equipped with closed-loop displacement transducer to control contact positioning between the cantilever and pivot.[14] In the current work, the hammerhead calibration required only the existing micro-positioning stages and overhead optical camera on the commercially available AFM instruments used (i.e., H dimensions at L^* were determined by hand and eye). The greatly improved precision in S_T determination was achieved as a consequence of two combined factors: First, the integrated hammerhead wings enable torque to be applied to the cantilever with much longer moment arms, which decreases the relative uncertainty of lever-arm length determination (H), and increases signal-to-noise due to larger torque; Second, a longer lever-arm enables a larger number of lever-arm lengths (H) to be utilized (i.e., more space), which allows for a larger variety of pivot measurements to be used in the data pool determining the resultant value.

Stiffness values for the experimental cantilever were measured using an instrumented indenter, which gave $k_Z = (16.3 \pm 0.1)$ N m^{-1} and $k_\phi = (500 \pm 18)$ nN m rad^{-1}. Using the indenter determined k_Z value, AFM pivot data were also used to measure k_ϕ. Listed in Table I, AFM Instrument A determined a k_ϕ value for the cantilever that was in agreement to within one standard error with the instrumented

indenter value, whereas AFM Instrument B exhibited a smaller k_ϕ that was outside one standard error agreement with the other two instruments (but within two standard errors). This weaker agreement was attributed to AFM Instrument B's smaller sensitivity to cantilever torque (S_T ≈ 0.17 V (nN m)$^{-1}$), which was more than a factor of 30 less sensitive than AFM Instrument A ($S_T \approx 6.1$ V (nN m)$^{-1}$). The large difference in optical lever sensitivity values observed for Instrument A compared to Instrument B is not surprising, since S_T and S_N^0 represent the state of an optical lever system for a given type of instrument and a given experimental setup. As these parameters tend to vary from one experimental setup to the next for any given instrument (for example, due to the specific cantilever used and the way it is mounted in the instrument), they are expected to vary quite significantly from one instrument design to the next (e.g., due to different laser sources, detector types, gains and filtering, and so on).

Crosstalk in an optical lever system can be observed directly from a pivot calibration plot, where the degree of crosstalk is observed from the intercept, $(\Delta V_L / \Delta V_N)_{H=0}$, at the zero-torque position, $H = 0$. In the calibration experiments reported in Fig. 7, optical crosstalk was observed to be $(\Delta V_L / \Delta V_N)_{H=0} = -0.023$ and $(\Delta V_L / \Delta V_N)_{H=0} = -0.008$ for Instrument A and Instrument B systems, respectively. As optical misalignment is a typical condition in LFM-type optical lever systems, this suggests that Eq. (8) should be modified to include an intercept term and a perhaps a slope correction for any effect that crosstalk may have on S_T. The impact of crosstalk on S_T pivot calibration data was analyzed in Appendix C, which found that crosstalk reduces the linearity of the optical lever response (required by Eq. (8) to determine S_T), while increasing uncertainty in the determination of S_T. However, for a system with an optical misalignment of magnitude typically encountered and practically reasonable, the effect of crosstalk turns out to be very small: the non-linear contribution is negligible and the additional uncertainty in S_T is on the order of 0.01 % to 1 % for crosstalk on the order of $0 < |(\Delta V_L / \Delta V_N)_{H=0}| \lesssim 10$ %. Systems with crosstalk larger than 10 % were not studied.

Two additional, related, factors suggest that optical misalignment will have a minimal effect on a pivot S_T calibration: First, the output ratio, $\Delta V_L / \Delta V_N$, accounts for the optical system response in both dimensions of the quad-cell PSD (Eq. (8));[12] Second, zero-torque measurements ($H = 0$) are acquired *in situ* with multiple torque measurements ($H \neq 0$) in the same calibration sequence.[13] Although a S_T calibration determines the optical lever system response to cantilever torque, the essential measurement in the calibration is the zero-torque measurement, which provides the normal sensitivity of the optical lever system, S_N^0. In combination with k_Z, S_N^0 provides a measurement of (normal) force, which facilitates a measurement of torque, via H. Note that a S_N^0 calibration is typically made without consideration of optical crosstalk, since the specific optical path traversed by the laser beam from the cantilever defines the optical lever response to pure flexure in the cantilever (in the absence of mechanical crosstalk). From this standpoint, since both dimensions of the quad-cell detector are accounted for in the optical response ($\Delta V_L / \Delta V_N$), and zero-torque measurements ($H = 0$)

are associated with multiple cantilever torque measurements ($H \neq 0$), the S_T calibration is seemingly insensitive to optical misalignment (provided that the linearity of the resultant optical response is unaffected, which, from analysis in Appendix C, turns out to be the case). Notwithstanding, experimental measurements should always be made within the linear response range of the PSD and multiple lever-arm (H) measurements should be made in conjunction with zero-torque measurements ($H = 0$), since the use of only a single lever-arm (torque) measurement, without incorporation of a zero-torque measurement *in situ* in the calibration,[12] can lead to large systematic errors, because the contribution of crosstalk to the calibration cannot be adequately known.

The effect of crosstalk on the uncertainty of a pivot torsional stiffness (k_ϕ) measurement can be observed directly from the k_ϕ pivot calibration plot, as shown in Figs. 8(a) and 8(b), where the optical response to cantilever torsion "splits" with magnitude and direction of cantilever twist. The source of the systematic error is revealed in Eq. (12), in which the lateral portion of the optical response is ignored in the calculation, meaning that alignment of the optical lever system is not taken into account. The misalignment is illustrated conceptually in Fig. 8(c). The effect of optical crosstalk on pivot k_ϕ measurements was analyzed in Appendix C, along with a numerical study demonstrating that the split optical response, caused by crosstalk, can be used to determine k_ϕ with a high degree of precision by performing a linear fit to all data—to obtain an "averaged" k_ϕ—as was done for the Fig. 8 data (Sec. III C).

The experimental work discussed in this paper demonstrated sub-percent statistical uncertainties for the determination of optical lever S_T values generated by the hammerhead pivot method. This high level of precision motivated a quantitative analysis of the accuracy potential of the technique, carried out here using the finite element method. For the experimental cantilever design used in this work, the simulation study produced three main findings. (1) At a distance $L*$ from the cantilever fixed end, where the cantilever flexural stiffness is k_Z, a z-directed load, F_Z, can be measured from the flexural deflection of the cantilever, regardless of whether the cantilever is loaded at a position that is coincident with the cantilever center of shear ($H = 0$), or whether F_Z is applied off-axis from the center of shear by a distance H (in the y-direction), with errors predicted to be less than 0.1 % for load positions extending $-70\,\mu$m $\leq H \leq +70\,\mu$m from the center of the cantilever head. (2) Head deformation was predicted to cause errors of ≈ 6 % in the determination of cantilever torsional stiffness by instrumented indentation measurements (analysis in Appendix B). (3) Head deformation during AFM pivot loading was predicted to cause errors on the order of ≈ 2 % in the determination of optical lever torque sensitivity (S_T), which carry through to result in errors of the same magnitude in the measurement of lateral (friction) forces. Findings (1) and (3) have a direct impact on the accurate quantification of LFM friction forces via the pivot calibration method. With regard to finding (1), as force makes its way into the pivot calibration by way of flexural deflection of the cantilever, this small estimated error demonstrates that the metrology underpinning the pivot calibration method is sound

in terms of the quantification of force and torque applied to a hammerhead cantilever via pivot (F_Z) loading. With regard to finding (3), the simulation study found that torque sensitivity errors were largely the result of deformation in the head of the hammerhead cantilever during pivot loading, despite it being unclear as to what degree such small deformations might produce actual experimental systematic errors in the AFM optical response (for different spot sizes and optical geometries). In any case, three possible methods to reduce or avoid the potential error source were proposed. The first suggestion was based on St. Venant's principal, such that reduced error could theoretically be obtained if optical detection were performed at some distance away from the applied load—on the "neck" rather than the "head" of the cantilever—albeit at the expense of optical lever sensitivity. A second analysis demonstrated that a significant reduction in error could be achieved via reduction in the length of the H lever-arm set used for the calibration (Fig. 11), albeit at the expense of greater relative uncertainty in H. A third possibility would be to fabricate a cantilever with a head that is somewhat thicker (and thence stiffer) than the rest of the cantilever, which would minimize head flexure in future cantilever designs. These possibilities were proposed because a reduction from say (2 to 3)% to (1 to 2)% or less is worth pursuing, as this type of error is not the only one that requires consideration. From Eq. (8), sub-percent uncertainties in both k_Z and S_N^0 determinations are achievable,[4] and uncertainties in H can be maintained at the percent-level, although such values will depend largely on the equipment and user performing the calibration.

In measuring friction via LFM and calibrating the optical lever system for such measurements, via Eq. (6), three major sources of uncertainty in the measurement of friction force, F_Y, are apparent. One source of uncertainty, via Eq. (6), will arise from the way in which the lateral deflection, ΔV_L, is calculated from friction-loop data, which will depend on the way in which experiments are conducted and how data are processed; for example, whether the lateral deflection "noise" in the dynamic (sliding) portions of friction-loop data (see Fig. 1(a)) is considered unimportant and thence averaged out, or whether it is the subject of a stick-slip friction investigation. A second source of uncertainty, via Eq. (6), is in the determination of the probe lever-arm length, h. Finite element modeling conducted here has revealed negligible displacement of the cantilever shear center for practically applicable lateral loads imposed on the hammerhead cantilever. In this case, the probe lever-arm, h, extends from the shear center of the cantilever to the point of contact between the probe and surface. For LFM measurements of friction using hammerhead cantilevers, fitted with integrated tips or colloidal probes, the largest source of uncertainty is likely to be in the length determination of the probe lever-arm, h, which requires the summation of two dimensional measurements that are made separately (*ex situ*) to all other measurements: (1) the half-thickness of the cantilever directly above the probe, and (2) the probe length, from its apex to the point at which it is connected to the cantilever. The third source of uncertainty, via Eq. (6), is in the determination of the optical lever torque sensitivity parameter itself, S_T, for which this paper has demonstrated precise determinations by way

of sub-percent statistical uncertainties. Currently, a significant contribution to S_T uncertainty comes from uncertainty in the determination of H. To a large extent, improved H measurements will come with improved fiducial markings and other features on a ramp chip that will allow better positioning, alignment and contact between the cantilever and ramp chip during pivot loading. Notwithstanding, an accurate determination of S_T, by Eq. (8), is achievable by way of a detailed characterization of the optical detection system for ΔV_N and ΔV_L and associated traceable determination of S_N^0 and of H and k_Z. These measurements will be carried out as part of standardization in future work.

The central focus of this paper has been on the calibration of AFM optical lever systems for the quantification of LFM friction-loop data using hammerhead cantilevers and the LFM pivot calibration method. There are, however, a number of other issues for the LFM experimentalist to consider in quantifying friction data, and although these issues fall outside the scope of the current paper, they warrant mention as considerations for experimental diligence (as well as focus topics for future work). One issue is the effect of optical lever system crosstalk on friction-loop measurements. The principal consequence of crosstalk is a convolution of normal and lateral PSD output as the cantilever deflects. During an LFM friction experiment, usual practice is to maintain a constant applied normal load during sliding. To do this, the experimentalist typically operates an instrument-controlled feedback loop that works by maintaining a constant pre-selected normal output (V_N*), often called the "setpoint." The imposed setpoint complicates the interpretation of normal load when optical crosstalk is present, since a change in lateral output (as the cantilever twists) will produce a change in normal output, V_N, which in turn will cause the active feedback loop to adjust the *apparent* load dynamically from one sliding (twisting) direction to the other. The implication is that the *actual* load, F_Z, will be changed rather than maintained, and that this change will be a function of the direction and magnitude of lateral deflection (cantilever twist). In addition, the torque applied to the cantilever will also be influenced by the load adjustment, according to the specific friction-load relationship between the probe and surface. In most cases, these effects are likely to be small, but not necessarily negligible. Also in regard to the interpretation and control of applied normal load, the angle at which an AFM cantilever is mounted in the instrument poses several issues for the LFM experimentalist, including: (1) the appropriate vector correction for the interpretation of normal force requires knowledge of the cantilever and probe angles relative to the experimental surface[8] (this adjustment is typically on the order of a few percent; for simplicity, such corrections were not made or included in equations in this paper). (2) For determination of optical lever normal sensitivity, attention should be paid to the interpretation of force-displacement ramp data, which is sometimes subject to hysteresis between approach and retract compliance slopes[7] (approach-retract hysteresis was statistically insignificant for all data observed in this work). (3) For both normal and lateral force measurements, it should be kept in mind that, as normal applied load is adjusted, the probe will displace axially (x-direction) on the surface.[28] In pursuit of accuracy in

LFM friction measurements, such issues should be addressed in future work.

The hammerhead cantilever design used in this paper has demonstrated a straightforward means of performing a precise optical lever torque sensitivity (S_T) calibration for LFM friction data. Finite element analysis of the cantilever has indicated that the pivot calibration method provides an accurate representation of cantilever mechanics, in which force and torque applied to the cantilever during pivot loading can be used to interpret force and torque applied to the cantilever during lateral (friction) loading, with an uncertainty on the order of about 2%, reducible via refinement of calibration methodology or cantilever design. The prospect offered by hammerhead-type cantilever designs and the associated pivot calibration method is that accurate LFM friction measurements could one day be made with a total uncertainty budget less than 5%.

ACKNOWLEDGMENTS

APPENDIX A: FURTHER DETAILS OF HAMMERHEAD CANTILEVER FINITE ELEMENT MODELING AND CALCULATIONS

Numerical modeling of the cantilever elastic response was performed using a commercially available finite element analysis software package. Three identical cantilever models were created, each consisting of standard 10-node quadratic tetrahedrons, and differing only in the density of elements. Using a free-meshing algorithm, the element linear dimensions for coarse, medium and fine meshes were set nominally to 12.5 μm, 6.25 μm, and 3.125 μm, respectively. To ensure doubling of the linear element density in the z-direction, the three cantilever meshes were manually divided into 2, 4, and 8 x-y-oriented slabs, respectively, for each mesh. The resulting numbers of elements for each mesh were about 1850 (coarse), 14 400 (medium) and 111 000 (fine) with slight variations depending on the force position.

All quantities were calculated using n-point polynomial Richardson extrapolation with assumed error of the form $\sigma(d) = \sum_{i=2}^{n+1} a_i d^i$, where d parameterizes the mesh coarseness: $d = 1$ (coarse), $d = 1/2$ (doubled once), $d = 1/4$ (doubled again) and a_i are fit to the numerical data.[26] Reported numerical errors in scalar outputs were estimated as the difference between the $n = 3$ Richardson extrapolation using all three meshes, and $n = 2$ Richardson extrapolation using the two coarser meshes. All mathematical operations such as algebra, numerical integration and regression analyses were performed prior to extrapolation, rather than performing algebra on extrapolated quantities (so that it was not necessary to guess the correlation of various errors; constructive error compounding or cancellation was taken into account

naturally via the extrapolation procedure and subsequent error estimation). As an example, the simulated pivot method calibration of S_T (Sec. IV C) had a number of intermediate quantities, such as k_θ, ϕ and θ. The full S_T simulation procedure was performed for each mesh resolution, resulting in three distinct estimates of S_T. Richardson extrapolation was then performed on the sequence of three S_T values to yield the best estimator and its associated numerical error.

All loads applied to cantilever models were point forces of magnitude, 5 μN. The point force approximation is convenient, but it potentially gives rise to mathematical singularities when meshes are refined to a very high degree. The resulting finite element models were thus semi-convergent with respect to element size. The element sizes (larger than 1 μm) were larger than a typical contact radius (<100 nm), and thus tended to underestimate the true contact compliance that was already known to be negligible (Sec. III B). The small estimated numerical errors demonstrated that the models were at the intermediate optimum scale at which point force divergences were appropriately cut off, but other contributions to calculated quantities were obtained to great numerical accuracy.

The finite element software flagged many elements as being highly distorted as they were "pancaked" in the plane of the cantilever. This distortion kept the problem numerically tractable; however, each refinement of the mesh included doubling the density in all three dimensions, and the resulting satisfactory numerical error estimates justified *ad hoc* the decision to ignore these warnings.

Numerical boundary integrals given in Eq. (13) were performed using 1D quadratic elements that were commensurate with the edges of 3D tetrahedral elements.

APPENDIX B: INDENTATION SIMULATIONS OF HAMMERHEAD CANTILEVER

Finite element simulations, analogous to instrumented indentation experiments (in Sec. III B), were performed using a larger number and range of moment lever-arms than experiment, extending in 5 μm increments from $H = 15$ μm to 70 μm across a wing ($H = y$ in Fig. 12). Displacement (in the z-direction) at the point of force application was used to determine compliance as a function of H. Analogous to experiment (Sec. III B), least-squares fitting to Eq. (10) was then performed for each mesh resolution to give stiffness values for k_Z and k_ϕ. Finally the best estimate and uncertainty errors were determined using Richardson extrapolation (Appendix A). The results are reported in Table III, where cantilever flexural stiffness, k_Z, via Eq. (10), was in agreement with its reference value (Table II) to within 0.2%; whereas the k_ϕ value, via Eq. (10), compared only to within 7 % of its reference value. In contrast to the quantification of k_Z, the explicit quantification of k_ϕ is not required for a pivot determination of S_T and the calibration of LFM lateral friction forces. However, the relatively large error associated with the simulated indenter determined k_ϕ value highlights a possible shortcoming in assumptions underlying the cantilever mechanical response to indentation loading; notably the completeness of Eq. (10).
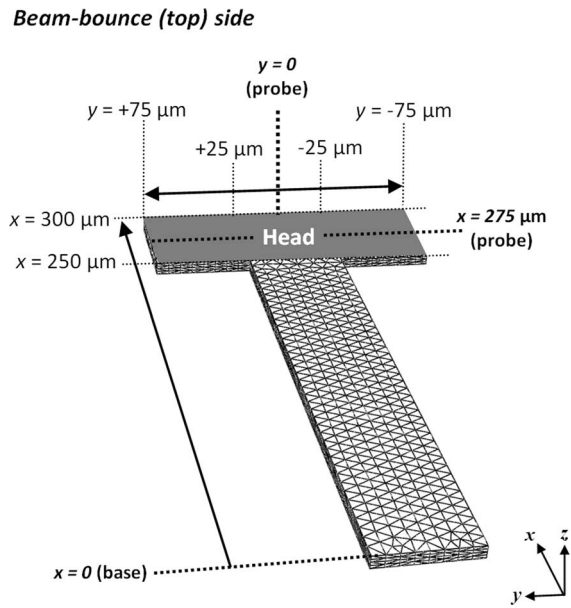
Beam-bounce (top) side

FIG. 12. Beam-bounce (top) side of hammerhead cantilever model.

The head deformation illustrated in Fig. 10(a) is largely due to flexure of the "wings" of the hammerhead cantilever during ΔZ (pivot) loading. This will be demonstrated in the following exercise, which aims to modify Eq. (10) to include a wing flexure term. The wing flexure deformation mode was approximated as a plane-strain beam running along the y-direction of the head. Referring to Fig. 12, head flexure is assumed to be qualitatively similar to the flexure of a uniform beam extending from $y = -75\ \mu$m to $y = +75\ \mu$m, which is pinned at $y = -25\ \mu$m and $y = +25\ \mu$m. The attachment of the head to the rest of the cantilever at $x = 250\ \mu$m is rather complicated to describe analytically, as the cantilever must satisfy both mechanical equilibrium and compatibility along the extent of the attachment from $y = -25\ \mu$m to $y = +25\ \mu$m. To simplify the analysis, the attachment (between the head and cantilever) was approximated as two fixed pin supports located at the extremes of the attachment (described below). The cantilever head flexure compliance $(k_w^H)^{-1}$ was calculated as the vertical displacement (w) per unit force at the point of loading ($y = H$) and added to the compliance terms in Eq. (10) to result in a more complete expression. In the following, the total compliance expression is formed by first deriving the wing compliance term, in Appendix B 1, and the appropriate elongation modulus, E, for bending of the cantilever neck and head, in Appendix B 2, before incorporation into the final expression, called the *double-pin supported beam compliance*, in Appendix B 3.

1. Wing compliance term

While deriving the compliance formula, beam dimensions are given symbolically (i.e., as variables). The y extents of the beam are $y = \pm l$, with $l = 75\ \mu$m. The pin supports are located at $y = \pm H_a$ with $H_a = 25\ \mu$m. The symbol H_a is chosen in anticipation of the final result, Eqs. (B1) and (B2) below. Additional model inputs are the effective elongation

modulus (E) and the cross-sectional areal moment (I). The beam cross-section is approximated as uniform and only takes into account the rectangular portion of the head; that is, the effects of the probe geometry on the areal moment (I) and resisting moment (M) are neglected.

Consider a beam extending from $y = -l$ to $y = l$ with two pin supports at $y = -H_a$ and $y = +H_a$. If the beam is loaded with an upward transverse force F_z at $y = H$, its compliance is the elastic curve displacement at $y = H$ per unit force, $\left(k_w^H\right)^{-1} = w(H)/F_z$. Applying Euler-Bernouli beam theory and using singularity functions, $\langle \ldots \rangle^n$, the resisting shear force (V) and bending moment (M) are:

$$V(y) = R_A \langle y + H_a \rangle^0 + R_B \langle y - H_a \rangle^0 + F_Z \langle y - H \rangle^0,$$

$$M(y) = R_A \langle y + H_a \rangle^1 + R_B \langle y - H_a \rangle^1 + F_Z \langle y - H \rangle^1,$$

where R_A and R_B are the mechanical constraint forces at $-H_a$ and $+H_a$, respectively, and $\langle x \rangle^n = (x)^n$ when $x > 0$, and $\langle x \rangle^n = 0$ when $x \leq 0$.[27] Mechanical equilibrium requires that the resisting shear force and moment each equal zero at the maximum y-coordinate of the beam ($y = l$) as there are no applied or constraint forces or couples there; and thus,

$$V(l) = R_A \langle l + H_a \rangle^0 + R_B \langle l - H_a \rangle^0 + F_Z \langle l - H \rangle^0$$
$$= R_A + R_B + F_Z = 0.$$
$$M(l) = R_A \langle l + H_a \rangle^1 + R_B \langle l - H_a \rangle^1 + F_Z \langle l - H \rangle^1$$
$$= (R_A + R_B + F_Z)l + R_A H_a - R_B H_a - F_Z H$$
$$= R_A H_a - R_B H_a - F_Z H = 0,$$

using the fact that the coefficient of l is simply the total resisting shear force ($V(l) = 0$). Solving for the reaction forces,

$$R_A = \frac{H - H_a}{2H_a}F_Z; \quad R_B = -\frac{H + H_a}{2H_a}F_Z.$$

Performing double integration on the resisting moment (M), $w(y) = (EI)^{-1}(\int dy)^2 M(y)$. Applying the constraints, $w(-H_a) = w(H_a) = 0$,

$$w(y) = \frac{F_z}{12EIH_a}\big[(H - H_a)\langle y + H_a \rangle^3 - (H + H_a)\langle y - H_a \rangle^3$$
$$+ 2H_a\langle y - H \rangle^3 - (H_a - y)\langle -(H_a + H) \rangle^3 - (H_a + y)$$
$$\times \langle H_a - H \rangle^3 + 4H_a^2(H_a - H)(H_a + y)\big].$$

Noting that by symmetry $k_w^H = k_w^{|H|}$, and considering the two cases $|H| \leq H_a$ and $|H| > H_a$,

$$\left(k_w^H\right)^{-1} = \frac{w(H)}{F_z}$$

$$= \frac{1}{6EI}\begin{cases} \left(H^2 - H_a^2\right)^2/H_a; & |H| \leq H_a \\ 2\left(|H| - H_a\right)^2\left(|H| + H_a\right); & |H| > H_a \end{cases}.$$
$$\text{(B1)}$$

This wing compliance term is added to the cantilever flexural and torsional compliances (Eq. (10)) to obtain the double-pin supported beam compliance expression in Appendix B 3 below. Preceding this, the value of the effective Young modulus,

E, to be used in the final expression, is calculated in Appendix B 2 below.

2. Elongation modulus

The appropriate elongation modulus E for bending of the cantilever neck and head is calculated as follows. Under flexure, in the $x(y)$-direction, i.e., bending about the $y(x)$-axis, the head is in an approximate state of plane-strain in the x-$z(y$-$z)$-plane which is a {110} plane. Flexure elongates material fibers in the $x(y)$-direction, a ⟨110⟩ direction. The effective elongation modulus is thus designated $E_{\{110\}\langle110\rangle}$. To calculate this modulus, the cubic elastic stiffness tensor was rotated 45° about the z-axis, a ⟨100⟩ direction. Then, the shear strains, the normal strain in the $y(x)$-direction, and the normal stress in the z-direction, were set to zero. Solving for the resulting ratio of stress to strain in the $x(y)$-direction, the required modulus was obtained:

$$E_{\{110\}\langle110\rangle} = \left(c_{11}^2 + c_{11}c_{12} - 2c_{12}^2 + 2c_{11}c_{44}\right)/(2c_{11}),$$

and in the case of silicon, $E_{\{110\}\langle110\rangle} = 169.8\,\text{GPa}$.

3. Double-pin supported beam compliance model

Incorporation of the appropriate effective Young modulus (calculated above) into Eq. (B1) above and adding this compliance expression to Eq. (10) results in a total compliance of

$$(k_Z^{\text{tot}})^{-1} = k_Z^{-1} + (k_\phi)^{-1}H^2 + a\frac{1}{6E_{\{110\}\langle110\rangle}I}$$

$$\times \begin{cases} \left(H^2 - H_a^2\right)^2/H_a; & |H| \le H_a \\ 2\left(|H| - H_a\right)^2\left(|H| + H_a\right) & |H| > H_a \end{cases}, \quad \text{(B2)}$$

where $H_a = 25\,\mu\text{m}$, $E_{\{110\}\langle110\rangle} = 169.8\,\text{GPa}$; I is the bending moment of inertia $(= (1/12)(50\,\mu\text{m})(6\,\mu\text{m})^3 = 900\,\mu\text{m}^4)$; and a is introduced as an artificial parameter. Theoretically, $a = 1$, but a can also be used as an additional fit parameter to adjust for the approximation of describing the head as a simple beam with simple supports, or perhaps for any uncertainty in the areal moment, I. Setting $a = 0$ recovers Eq. (10). Fig. 13 shows the simple beam model, loaded at $H = 40\,\mu\text{m}$, exhibiting a mechanical deformation that is qualitatively similar to the displacement difference, $\vec{u}_{\text{point}} - \vec{u}_{\text{uniform}}$, in Fig. 10(a). Note that in both cases, the head responds to a pivot load such that the opposite wing pitches up as the other is loaded, forming a slight trough in the center of the head. The appropriate boundary conditions are zero-displacement at $y = \pm25\,\mu\text{m}$, since Eq. (10) already accounts for compliance due to rotation about the x-axis (ϕ) and the y-axis (θ).

The results of using Eq. (B2) to fit the simulated indentation loading data are compared to those of Eq. (10) in Table III, benchmarked against reference values $(k_Z)_{\text{exact}}$ and $(k_\phi)_{\text{exact}}$ (Table II). From Table III, the determination of cantilever flexural stiffness, k_Z, via simulated indentation is well approximated by all expressions, with values comparing to $(k_Z)_{\text{exact}}$ to within: 0.2 % when wing flexure is neglected (i.e., Eq. (10), or Eq. (B2) with $a = 0$); 0.01 % for Eq. (B2), with $a = 1$; and 0.04 % for Eq. (B2), with
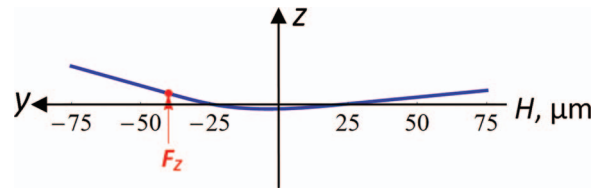

FIG. 13. (Color online) Plot of the double-pin supported beam model (arbitrary z scale), used to account for head deformation in indentation loading.

a used as a fit parameter. For the determination of cantilever torsional stiffness, however, when wing flexure is neglected ($a = 0$ or Eq. (10)), k_ϕ compared to its reference value $((k_\phi)_{\text{exact}})$ only to within 7 %, whereas estimated bounds of <1 % and <2 % were obtained using Eq. (B2) for cases where $a = 1$ and where a was used as fit parameter, respectively.

From these results it is clear that for the hammerhead cantilever design used in this study, the measurement of flexural stiffness at L^* can be determined using multiple instrumented indentation measurements across the head of the hammerhead cantilever, with errors of <1 %, without the need to account for wing flexure in the measurement model. On the other hand, if a torsional stiffness measurement is required, wing flexure must be accounted for in any model used to fit indentation force-displacement data in order for measurement errors to be < 1 %.

APPENDIX C: EFFECT OF OPTICAL LEVER SYSTEM CROSSTALK ON THE PIVOT CALIBRATION METHOD

Optical misalignment is caused by misalignment between the cantilever reflective (beam bounce) surface and the sector axis of the PSD. This condition complicates the interpretation of forces acting on the cantilever, since normal and lateral output signals from the PSD are convoluted, creating a "crosstalk." The following describes an analysis of PSD crosstalk and its effect on the pivot LFM calibration method. To simulate crosstalk, an optical lever system model is introduced in Appendix C 1, such that both normal and lateral channels contain both normal and lateral contributions. This model is used to study the effect of crosstalk on the pivot method for the determination of torque sensitivity in Appendix C 2, and on the determination of cantilever torsional stiffness in Appendix C 3.

1. Optical lever system model

To describe an optical lever system in which cross-talk causes both normal and lateral channels to respond to a given input, the following model is written in terms of normal force F_Z and torque T on the cantilever, by modifying Eq. (7), such that

$$\Delta V_{\text{N}} = S_{\text{N}}^0 k_Z^{-1} F_Z + S_{\text{NT}} T, \quad \text{(C1a)}$$

$$\Delta V_{\text{L}} = S_{\text{T}} T + S_{\text{TN}} k_Z^{-1} F_Z, \quad \text{(C1b)}$$

where k_Z is the flexural stiffness of the cantilever and F_Z is the normal force applied to it (Eq. (1)), S_{N}^0 is the normal

displacement sensitivity (Eq. (2)) and S_T is the torque sensitivity (Eq. (5)) of the optical lever system. The system has two crosstalk terms: S_{NT} is a coefficient with units of $V(Nm)^{-1}$ that characterizes how cantilever torque alters the normal output, and S_{TN} is a coefficient with units of Vm^{-1} that characterizes how cantilever normal force alters the lateral output. Note that Eqs. (C1) are valid when the PSD responds proportionately to the normal force and torque, and represents a general description of cross-talk, regardless of the source (e.g. optical, mechanical).

2. Torque sensitivity calibration

The key calibration equation in this paper—Eq. (8)—describes a means to obtain a S_T calibration of the optical lever system, generated by the system output response, $(\Delta V_L / \Delta V_N)$, to cantilever torque via various lever-arms, H. Accepting that a LFM optical lever system is almost always subject to misalignment, then Eq. (8) should be regarded as a simplification of a more general form. Upon some rearranging of Eq. (C1), the output ratio can be expressed as

$$\frac{\Delta V_L}{\Delta V_N} = \frac{H\left(\frac{k_Z}{S_N^0}\right) S_T + \frac{S_{TN}}{S_N^0}}{1 + H\left(\frac{k_Z}{S_N^0}\right) S_{NT}}. \quad (C2)$$

Expanding Eq. (C2) in powers of $\left(\frac{k_Z}{S_N^0}\right)$,

$$\frac{\Delta V_L}{\Delta V_N} = \frac{S_{TN}}{S_N^0} + \left(S_T - \frac{S_{TN} S_{NT}}{S_N^0}\right)\left(\frac{k_Z}{S_N^0} H\right)$$
$$- S_{NT}\left(S_T - \frac{S_{TN} S_{NT}}{S_N^0}\right)\left(\frac{k_Z}{S_N^0} H\right)^2 + \cdots \quad (C3)$$

It is clear that the output ratio deviates from linearity by a term proportional to $S_{NT}(S_T - \frac{S_{TN} S_{NT}}{S_N^0})$. It turns out that this number is very small compared to other terms in Eq. (C3). Indeed, inspection of the S_T calibration plots in Fig. 7 shows that the $\frac{\Delta V_L}{\Delta V_N}$ vs. $H(\frac{k_Z}{S_N^0})$ relationship was very linear in the case of both instruments studied. In fact, based on the data presented in this paper, as well as other data obtained from a number of other S_T calibration experiments conducted using different hammerhead cantilevers and AFM instruments (data not reported here), the Pearson Correlation for a S_T calibration plot is typically observed to be $R^2 = 0.99$ or better. Considering this and turning attention to the linear term in Eq. (C3), there is a clear difference from Eq. (8) by a term referred to here as the "cross-talk error": $\Delta S_{T_{crosstalk}} = -\frac{S_{TN} S_{NT}}{S_N^0}$. This error contains the product $S_{TN} S_{NT}$ and is second order in crosstalk (so that if the relative effect of crosstalk on individual PSD output is small, the crosstalk error will be smaller still). Using experimental data and the equations provided above, a simple calculation demonstrates that $\Delta S_{T_{crosstalk}}$ is typically very small compared to S_T ($<1\%$), thereby justifying rigorously Eq. (8)—albeit modified by non-zero intercept term (S_{TN}/S_N^0), which has no effect on the quantification of LFM friction data. The following outlines a numerical analysis that further compares the magnitude of $\Delta S_{T_{crosstalk}}$ with S_T.
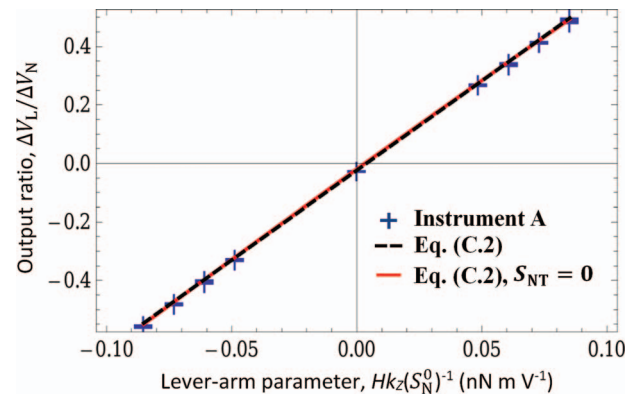

FIG. 14. (Color online) Pivot torque sensitivity output data comparison between Instrument A data and linear response models.

a. Numerical analysis

Figure 14 shows a comparison of three types of linear fits for a torque sensitivity (S_T) measurement, based on the "Instrument A" experimental data (Fig. 7; Sec. III; note that the normal sensitivity value, $S_N^0 = 1.34 \times 10^7\,V\,m^{-1}$, was determined experimentally; Table I). The cross marks show the instrument generated data, from which a linear fit gave a slope of $S_T = 6.14 \times 10^9\,V(Nm)^{-1}$ (Table I). The dashed line represents a fit of Eq. (C2) to $\frac{\Delta V_L}{\Delta V_N}$ vs. $(\frac{k_Z}{S_N^0} H)$, using S_T, S_{NT} and S_{TN} as fit parameters, which gave $S_T = 6.12 \times 10^9\,V(Nm)^{-1}$, $S_{NT} = 1.75 \times 10^8\,V(Nm)^{-1}$ and $S_{TN} = -2.67 \times 10^5\,V\,m^{-1}$. The solid line represents a fit of 'linearized' Eq. (C2), where $S_{NT} \to 0$ (i.e., Eq. (8) with a non-zero intercept, S_{TN}/S_N^0), which gave $S_T = 6.13 \times 10^9\,V(Nm)^{-1}$ and $S_{TN} = -3.21 \times 10^5\,V\,m^{-1}$. All fits are very linear (with adjusted R^2 values of at least 0.99) and all S_T values compare to within 0.5 %. Optical crosstalk in the instrument A system was $(\Delta V_L / \Delta V_N)_{H=0} = S_{TN}/S_N^0 = -0.023$. The same numerical exercise has also been conducted for other optical lever system data, but with much larger crosstalk values—on the order of $(\Delta V_L / \Delta V_N)_{H=0} = 0.1$ (data not reported here)—and even for these systems, the torque sensitivity data showed extremely good linearity, with crosstalk errors ($\Delta S_{T_{crosstalk}}$) that were $<1\%$ of S_T.

3. Cantilever torsional stiffness measurement

In the pivot method, k_ϕ is inferred to be the multiplicative inverse of the slope of $(S_N^0 / S_N^H) - 1$ vs. $k_Z H^2$ (Eq. (12)). Analysis of data in Fig. 8 assumed that the effects of the crosstalk could be removed by using the average of S_N^H values for both $H > 0$ and $H < 0$. Analogous to the formulation of Eq. (12), but introducing crosstalk terms into the analysis, Eqs. (C1a) and Eqs. (9) and (10), (11a) combine with $T = HF_Z$ to give

$$\frac{S_N^0}{S_N^H} - 1 = \frac{S_N^0 (k_Z H^2) - k_\phi k_Z S_{NT} H}{k_\phi \left(S_N^0 + k_Z S_{NT} H\right)}. \quad (C4)$$

If one then assumes that $S_{NT} \to 0$, Eq. (12) is recovered; however if $S_{NT} \neq 0$, Eq. (C4) differs from Eq. (12) and is not linear in $k_Z H^2$. From inspection of Fig. 8, the method of averaging the $H > 0$ and $H < 0$ responses to remove
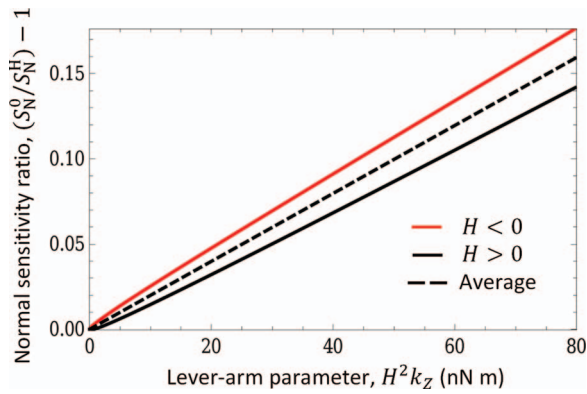
FIG. 15. (Color online) Pivot torsional stiffness measurement simulated using the linear response model, showing $H > 0$, $H < 0$, and average modeled linear responses.

crosstalk effects appears to be valid, but it is worthwhile to check if such an approach is consistent with the linear response model. Using $H = \pm|H|$ and taking the average,

$$\overline{\frac{S_N^0}{S_N^{|H|}} - 1} = \frac{1}{2}\left[\left(\frac{S_N^0}{S_N^{+|H|}} - 1\right) + \left(\frac{S_N^0}{S_N^{-|H|}} - 1\right)\right]$$

$$= \frac{1 + \frac{k_\phi k_Z S_{NT}^2}{S_N^{0^2}}}{1 - \frac{k_Z S_{NT}^2}{S_N^{0^2}}(k_Z H^2)} \frac{1}{k_\phi}(k_Z H^2). \quad (C5)$$

Expanding in powers of $(k_Z H^2)$,

$$\overline{\frac{S_N^0}{S_N^H} - 1} = \left(\frac{1}{k_\phi} + \frac{k_Z S_{NT}^2}{S_N^{0^2}}\right)(k_Z H^2) + \frac{k_Z S_{NT}^2}{S_N^{0^2}}$$

$$\times \left[\frac{1}{k_\phi} + \frac{k_Z S_{NT}^2}{S_N^{0^2}}\right](k_Z H^2)^2 + \cdots. \quad (C6)$$

Note, that the coefficient of $k_Z H^2$ differs from $1/k_\phi$, creating an error: $\Delta(k_\phi^{-1})_{crosstalk} = \frac{k_Z S_{NT}^2}{S_N^{0^2}}$. If this term is small compared to $1/k_\phi$ one can see that the nonlinear term is similarly small, and Eq. (12) is a reasonable approximation.

a. Numerical analysis

From the Instrument A data, Eq. (C4) was used to simulate the instrument response using $S_N^0 = 1.34 \times 10^7$ V m^{-1}, $S_T = 6.14 \times 10^9$ V (N m)$^{-1}$, $k_Z = 16.3$ N m^{-1}, and $k_\phi = 5.03 \times 10^{-7}$ N m rad^{-1} (Table I), and $S_{NT} = 1.75 \times 10^8$ V (N m)$^{-1}$, $S_{TN} = -2.67 \times 10^5$ V m^{-1}. A plot of $\frac{S_N^0}{S_N^H} - 1$ vs. $k_Z H^2$ is shown in Fig. 15, which gives the same form that was observed in Fig. 8. The data in Fig. 8 do not include data near $H = 0$ and the plot appears linear (for small H, however, the simulation reveals that the response is more like a distorted, tilted parabola). Averaging the response for positive and negative H appears very linear; thus, the nonlinearity in Eq. (C5) can be reasonably neglected.

Numerically, the resulting inverse slope was $k_\phi = 5.02 \times 10^{-7}$ N m rad^{-1}, which compared with the input value of $k_\phi = 5.03 \times 10^{-7}$ N m rad^{-1}, gives a systematic error of 0.2 %.

[1]M. P. de Boer and T. M. Mayer, MRS Bull. **26**(4), 302 (2001); S. H. Kim, D. B. Asay, and M. T. Dugger, Nanotoday **2**(5), 22 (2007).

[2]A. Khurshudov and R. J. Waltman, Wear **251**, 1124 (2001); H. F. Hamann, M. O'Boyle, Y. C. Martin, M. Rooks, and H. K. Wickramasinghe, Nature Mater. **5**, 383 (2006); R. J. Cannara, B. Gotsmann, A. Knoll, and U. Durig, Nanotechnology **19**, 395305 (2008); E. Gnecco, Nature (London) **461**, 178 (2009).

[3]Y. Min, M. Akbulut, K. Kristiansen, Y. Golan, and J. Israelachvili, Nature Mater. **7**, 527 (2008).

[4]M.-S. Kim and J. R. Pratt, Measurement **43**, 169 (2010).

[5]C. P. Green, H. Lioe, J. P. Cleveland, R. Proksch, P. Mulvaney, and J. E. Sader, Rev. Sci. Instrum. **75**(6), 1988 (2004); G. A. Matei, E. J. Thoreson, J. R. Pratt, D. B. Newell, and N. A. Burnham, Rev. Sci. Instrum. **77**, 083703 (2006); C. A. Clifford and M. P. Seah, Meas. Sci. Technol. **20**, 125501 (2009).

[6]B. Cappella and G. Dietler, Surf. Sci. Rep. **34**, 1 (1999); H.-J. Butt, B. Cappella, and M. Kappl, Surf. Sci. Rep. **59**, 1 (2005).

[7]Due to the mounted angle of an AFM cantilever and probe relative to a surface, frictional probe–surface interactions can sometimes produce statistically significant hysteresis between approach and retract compliance slopes of force-displacement curves. For example, see: G. S. Watson, B. P. Dinte, J. A. Blach-Watson, and S. Myhra, Appl. Surf. Sci. **235**, 38 (2004); J. Stiernstedt, M. W. Rutland, and P. Attard, Rev. Sci. Instrum. **76**, 083710 (2005); J. Stiernstedt, M. W. Rutland, and P. Attard, Rev. Sci. Instrum. **77**, 019901 (2006); J. R. Pratt, G. A. Shaw, L. Kumanchik, and N. A. Burnham, J. Appl. Phys. **107**, 044305 (2010).

[8]The vector correction for normal force requires knowledge of the cantilever and probe angles relative to the surface. For example, see: S. A. Edwards, W. A. Ducker, and J. E. Sader, J. Appl. Phys. **103**, 064513 (2008).

[9]O. Marti, J. Colchero, and J. Mlynek, Nanotechnology **1**, 141 (1990); G. Meyer and N. M. Amer, Appl. Phys. Lett. **57**(20), 2089 (1990).

[10]M. Munz, J. Phys. D: Appl. Phys. **43**, 063001 (2010).

[11]G. Bogdanovic, A. Meurk, and M. W. Rutland, Colloids Surf., B **19**, 397 (2000).

[12]A. Feiler, P. Attard, and I. Larson, Rev. Sci. Instrum. **71**(7), 2746 (2000).

[13]M. G. Reitsma, Rev. Sci. Instrum. **78**, 106102 (2007).

[14]K.-H. Chung and M. G. Reitsma, Rev. Sci. Instrum. **81**, 026104 (2010).

[15]S. P. Timoshenko and J. N. Goodier, *Theory of Elasticity*, 3rd ed. (McGraw-Hill, New York, 1982).

[16]R. W. Carpick, D. F. Ogletree, and M. Salmeron, App. Phys. Lett. **70**(12), 1548 (1997).

[17]R. W. Carpick and M. Salmeron, Chem. Rev. **97**, 1163 (1997).

[18]J. E. Sader and C. P. Green, Rev. Sci. Instrum. **75**(4), 878 (2004); K.-H. Chung, J. R. Pratt, and M. G. Reitsma, Langmuir **26**(2), 1386 (2010).

[19]M. A. Lantz, S. J. O'Shea, A. C. F. Hoole, and M. E. Welland, Appl. Phys. Lett. **70**(8), 970 (1997).

[20]J. D. Holbery, V. L. Eden, M. Sarikaya, and R. M. Fisher, Rev. Sci. Instrum. **71**(10), 3769 (2000).

[21]Z. C. Ying, M. G. Reitsma, and R. S. Gates, Rev. Sci. Instrum. **78**, 063708 (2007).

[22]Uncertainties represent the resolution of the microscope used.

[23]R. E. Walpole and R. H. Myers, *Probability and Statistics for Engineers and Scientists* (Macmillan, New York, 1972); Unless otherwise stated, all uncertainties derived from linear least-squares fitting are standard errors of the fits.

[24]H. J. McSkimin and P. Andreatch, J. App. Phys. **35**(7), 2161 (1964).

[25]R. D. Cook, D. S. Malkus, M. E. Plesha, and R. J. Witt, *Concepts and Applications of Finite Element Analysis*, 4th ed. (Wiley, New York, 2001).

[26]D. C. Joyce, SIAM Rev. **13**, 435 (1971).

[27]R. C. Hibbeler, *Mechanics of Materials*, 7th ed. (Pearson Prentice Hall, Upper Saddle River, NJ, 2008).

[28]R. J. Cannara, M. J. Brukman, and R. W. Carpick, Rev. Sci. Instrum. **76**, 053706 (2005).